Customized light sheet microscope for rapid quality control of midbrain organoids during early development stages

Junqing Jiang

Department of Chemical Engineering

McGill University

Montreal, Quebec, Canada

April 2023

A thesis submitted to McGill University in partial fulfillment of the requirements for the degree of Master of Science

©Junqing Jiang 2023

Abstract

Oblique Plane Microscope (OPM) system is an emerging variation of light-sheet microscopy that offers ultra gentle illumination, versatile mounting options and rapid volumetric imaging speed to probe 3D tissue structures. Fluorescent microscopy has long been an important and powerful tool for the biological sciences due to its capability to differentiate subcellular components at high resolution. However, when applied to the field of tissue engineering, where we need to image cellular behaviour in large 3D structures, traditional confocal microscopy is severely limited in image acquisition speed at depth, while avoiding sample photobleaching. In contrast, light-sheet microscopy can achieve faster imaging throughput and lower photobleaching but suffers from limited tissue mounting options. OPM system were developed to address this limitation, as they utilize one single objective for both illumination and image acquisition, which allows for a wide range of sample preparation formats. Adding one rotational scanning mirror allows for fast optical slicing, and hence enables quick scanning of large tissues. Therefore, OPM systems present significant advantages for applications such as rapid quality control in brain organoid processing.

This equipment development thesis provides a complete, step-by-step recipe to build, control and operate a customized OPM system based on Swept Confocally-Aligned Planar Excitation (SCAPE 2.0) microscope, with sample mounting options designed for quality control analysis of developing brain organoids. The system was designed to house three commonly used colour channels, Blue Fluorescent Protein (BFP) with excitation/emission at 375/460nm, Green Fluorescent Protein (GFP) at 488/525nm and Red Fluorescent Protein (RFP) at 561/620nm. In addition, a bright-field imaging system for sample location was customized and a commercial zoom lens was utilized to achieve magnifications ranging from 9.31X to 26.67X. Finally, the system was synchronized using MATLAB to achieve maximum imaging throughput. The imaging capabilities of the customized OPM system were demonstrated by using midbrain organoids during early developmental stages at which neural rosettes first form. The results showed that imaging depth of more than 200 μm can be achieved with laser power as low as 3 mW and exposure time as short as 10 ms. Such results were comparable to those obtained from the much more time-consuming process of optically clearing brain organoids, and imaging them using conventional confocal microscopy. Overall, this works provides a road map for novices to construct a low cost OPM system with capabilities to rapidly and gently image structures within large, versatile tissue samples.

Résumé

Le système de microscope à plan oblique (OPM) est une variation émergente de la microscopie à feuille de lumière qui offre une illumination ultra douce, des options de montage polyvalentes et une vitesse d'imagerie volumétrique rapide pour sonder les structures tissulaires 3D. La microscopie fluorescente a longtemps été un outil important et puissant pour les sciences biologiques en raison de sa capacité à différencier les composants subcellulaires à haute résolution. Cependant, lorsqu'elle est appliquée au domaine de l'ingénierie tissulaire, où nous devons imaginer le comportement cellulaire dans de grandes structures 3D, la microscopie confocale traditionnelle est gravement limitée en termes de vitesse d'acquisition d'image en profondeur, tout en évitant le photoblanchiment de l'échantillon. En revanche, la microscopie à feuille de lumière peut atteindre un débit d'imagerie plus rapide et un photoblanchiment moindre, mais souffre d'options de montage tissulaire limitées. Les systèmes OPM ont été développés pour remédier à cette limitation, car ils utilisent un seul objectif pour l'éclairage et l'acquisition d'image, ce qui permet une large gamme de formats de préparation d'échantillons. L'ajout d'un miroir de balayage rotatif permet une découpe optique rapide et donc un balayage rapide de grands tissus. Par conséquent, les systèmes OPM présentent des avantages significatifs pour des applications telles que le contrôle de qualité rapide dans le traitement d'organoïdes cérébraux.

Cette thèse de développement d'équipement fournit une recette complète et étape par étape pour construire, contrôler et faire fonctionner un système OPM personnalisé basé sur un microscope d'Excitation Planaire Confocale Alignée Balayée (SCAPE 2.0), avec des options de montage d'échantillons conçues pour l'analyse de contrôle de qualité des organoïdes cérébraux en développement. Le système a été conçu pour abriter trois canaux de couleur couramment utilisés, la protéine fluorescente bleue (BFP) avec une excitation/émission à 375/460 nm, la protéine fluorescente verte (GFP) à 488/525 nm et la protéine fluorescente rouge (RFP) à 561/620 nm. De plus, un système d'imagerie en champ clair pour la localisation d'échantillons a été personnalisé et une lentille de zoom commerciale a été utilisée pour atteindre des agrandissements allant de 9,31X à 26,67X. Enfin, le système a été synchronisé à l'aide de MATLAB pour atteindre un débit d'imagerie maximal. Les capacités d'imagerie du système OPM personnalisé ont été démontrées en utilisant des organoïdes de la région mésencéphalique pendant les premiers stades de développement, au cours desquels les rosettes neurales se forment pour la première fois. Les

résultats ont montré qu'une profondeur d'imagerie de plus de 200 μm peut être atteinte avec une puissance laser aussi faible que 3 mW et un temps d'exposition aussi court que 10 ms. De tels résultats étaient comparables à ceux obtenus à partir du processus beaucoup plus long de clarification optique des organoïdes cérébraux et de leur imagerie en utilisant une microscopie confocale conventionnelle. Dans l'ensemble, ce travail fournit une feuille de route pour les novices pour construire un système OPM à faible coût avec des capacités pour imager rapidement et en douceur les structures dans de grands échantillons de tissus polyvalents.

Acknowledgement

First and foremost, I would like to thank my supervisor Dr. Christopher Moraes. Thank you for accepting me into the lab and put in so much faith on me – who have not had a class on optics ever since middle school – to take on such a microscope development project that costs insane amount of money. Up until today, I still question myself occasionally that how I managed to get into the group in the first place and managed to complete this project. Although I will probably never have a definite answer, but I know your guidance on both my academic and personal development is a huge part of the reason. Your encouragement and actions to actively find me external help on microscopy at the one-year mark of my degree was no doubt the turning point of everything.

Thank you to everyone in Moraes Lab, it was a great time working with all of you. Camille, Christina and Karthick, thank you for providing me with biological samples for both testing and verifying my microscope. Christina and Sabra, thank you for your patience when listening to my rambling and not obliterate me when I occasionally break the lab safety rule. Nic, thank you for helping me troubleshooting the cell culture. Chen and Ben, thank you for making the lab a fun place to work in.

Furthermore, I also want to give a very special thanks to Alfred and Bingying. This project will never close to be completed without your very kind help and teaching. It was both of you made me realize how welcoming and supportive the microscopy community can be. Alfred, your enthusiasm and contribution to the open-source science really reminds me the type of scientists I have been imagining since a child. With all the help I have received from both of you, it inspired me to keep working on advanced microscopy in the foreseeable future.

I also want to give a unique thanks to Xingyue. To me, that non-academic, extracurricular project we have accomplished is no less important compared to my microscope. And it could only be completed by us together.

Lastly, I want to give my most sincere thanks to my parents. If I were to detail everything, it could be another thesis by itself, so just going to keep things simple here. Thank you for all the freedom and support you two have provided to me in the past 25 years. If a child and parents really chose each other at the birth, it must be the best choice I have ever made.

Contribution of Authors

The data and analysis presented in this work was solely obtained by the author. Both midbrain organoids and its associated images on commercial confocal microscope systems after tissue-clearing were provided by Camille Cassel de Camps, who worked on these experiments in collaboration with Dr. Thomas Durcan at the Montreal Neurological Institute. This thesis was primarily written by the author and kindly edited by Dr. Christopher Moraes.

List of Figures and Tables

Contents

1. Introduction

1.1. Motivation

Fluorescent light has long been an important and powerful tool in biological science due to its capability to differentiate subcellular components with high resolution and a superior signal-to-noise ratio. However, with the advancement of tissue engineering and the growing interest in studying disease progression processes using 3D in-vitro tissue models, traditional confocal microscopes are severely limited in terms of achievable imaging depth, volumetric imaging throughput, and high photobleaching.

ne typical example is the quality control of midbrain organoids during early development stages. Derived from induced pluripotent stem cells (iPSCs), brain organoids have shown the capability to self-organize and recreate aspects of human embryonic development processes[1–5]. Thus, they have become emerging tools for facilitating the understanding of neural development and disease progression processes. However, the complex nature of stem cell development leads to severe heterogeneity in the brain organoids obtained during mass production, causing significant economic loss and logistical challenges.

To better facilitate the quality control of brain organoids using confocal microscopes, tissue-clearing techniques are commonly applied. Although these techniques significantly enhance the quality of the obtained images, the tissue clearing protocol requires up to two weeks to be completed[6,7], making it unfavorable for rapid quality control purposes. Furthermore, the use of the point scanning method greatly limits the volumetric imaging speed and induces overwhelming photobleaching[8,9]. The unwanted cone-shaped volumetric illumination above and below the focal point also generates unwanted photon-matter interactions, thereby decreasing both the achievable imaging depth and signal-to-noise ratio.

In contrast to the point scanning used by confocal microscopy, light sheet microscopy utilizes a thin sheet of light to illuminate the entire plane of interest within 3D tissue samples. This is achieved by using two orthogonally placed objectives, one for illumination and one for image detection. The planar illumination significantly increases the volumetric imaging throughput and reduces photobleaching[8–10]. However, the utilization of dual objectives poses challenges for sample handling and mounting options.

To create a more user- and sample-friendly 3D fluorescent microscope while retaining the advantages of light sheet microscopy, oblique plane microscopy (OPM) was developed[11]. By using a light sheet at an inclined angle, both sample illumination and image detection can be achieved using a single objective. Furthermore, spherical aberration and imaging plane defocusing can be optically corrected by introducing a remote refocusing system[11–13], resulting in isotropic, aberration-free images.

Building upon OPM, SCPAE 2.0 was developed by incorporating a galvo mirror for optical scanning and a commercial zoom lens for magnification adjustment[13]. This enables faster and finer scanning step resolution by avoiding scanning using the sample stage. Additionally, the use of a zoom lens resolves the constraint of fixed magnification imposed by the nature of the remote refocusing system, allowing different magnifications to be applied based on the needs of biological samples. Overall, SCAPE 2.0 overcame the significant mechanical complexity presented in the original OPM design.

As a result, it is proposed that a customized light sheet microscope based on SCAPE 2.0, along with dedicated control, automation algorithms, and post-processing pipelines, could better suit the need for rapid quality control of midbrain organoids during early development stages.

1.2. Aims and Objectives

The aim of this thesis was to develop a customized light sheet microscope based on OPM to facilitate rapid quality control of midbrain organoids during early development stages. To achieve this, the specific aims of this project were as follows:

1. Customize, assemble, calibrate, and characterize a light sheet microscope based on the principles of OPM.

2. Develop a control and automation strategy to enhance high volumetric imaging throughput.

3. Set up a post-processing pipeline specifically tailored for images obtained using the customized OPM.

2. Background and Literature Review

2.1. Fluorescent Microscopy

A fluorophore is a type of chemical compound capable of emitting light at certain wavelengths after absorbing light from a different wavelength.[14,15] The performance of a fluorophore is commonly evaluated by examining its excitation/emission band, which describes the required light source for excitation and the resulting emitted fluorescent light. By binding fluorophores to antibodies, it becomes possible to target specific cellular components, enabling fluorescent microscopy to probe physiological behavior at high resolution and even in real-time.[9]

Currently, there are multiple criteria used for classifying fluorescent microscopes. One common classification method is based on the capability to image samples with different thickness, distinguishing between 2D (epifluorescence) and 3D (confocal and light sheet) fluorescent microscopes. Fluorescent microscopes can also be differentiated based on the achievable resolution. The resolution of a light microscope is typically limited by the diffraction limit (~200nm, described by Ernst Abbe), while techniques that surpass this limitation, such as structured illumination[16], stimulated emission depletion[17,18] and single molecule localization[19], are referred to as super resolution microscopy. Furthermore, fluorescent microscopy can be classified based on their illumination mechanisms, including single photon, two-photon[20] and multi-photon[21] excitation.

The development of a fluorescent microscope involves a delicate balance between various factors, including spatial resolution, temporal resolution, signal-to-noise ratio (SNR), as well as limitations imposed by photobleaching and sample mounting options.

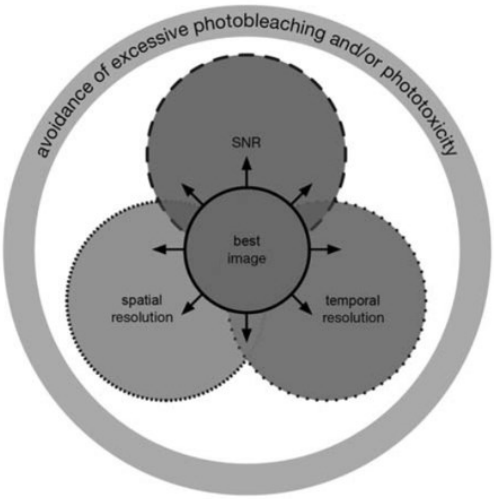

Figure 1 Balance and constraint for an optimal fluorescent microscope. Image is reproduced with permission from Combs et al.[9]

2.1.1. Parameters of performance and comparison of different microscopy

With the rapid development in the field of fluorescent microscopy, the boundaries between different designs can become blurred, making categorization difficult. As a result, spatial resolution, temporal resolution, penetration depth, photobleaching, and cost have become common parameters used to compare the performance of microscopes. Spatial resolution defines the level of detail that can be extracted by the microscope and can be further divided into resolution on the XY plane and the Z-axis. On the other hand, temporal resolution determines the imaging throughput.

To provide a comprehensive understanding of different microscopy techniques, Table 1 compares the prevalent parameters between commonly used 2D and 3D microscopy. The details of each type of microscope will be presented in the following sections. It should be noted that super-resolution microscopy, which surpasses the diffraction limit, has been excluded from this project due to its applications being beyond the scope of this project.

Table 1 Comparison between commonly used 2D and 3D microscopy[9]

	XY resolution	Z resolution	Penetration depth	Temporal resolution	Photobleaching	Cost
Epifluorescence	Diffraction limited	Poor (~1μm)	Poor	Best	Near non-existence	Low
Total internal reflection fluorescence (TIRF)	Diffraction limited	Diffraction limited	Poor (<300nm)	Good	Very low	Medium
Line scanning confocal (LSCM)	Close to 2× diffraction limit	~700nm	Good (<100 μm)	Good	High	Medium to high
Spinning disk confocal (SDCM)	Close to 2× diffraction limit	Worse than LSCM	Good (worse than LSCM)	Good (better than LSCM)	Moderate to high	Medium to high
Light-sheet fluorescence	Diffraction limited (depends on objective lens)	Good (depends on objective lens)	Best (up to hundreds of μm	Best	Low	Medium to high

2.2. Confocal Microscopy

Confocal microscopy is currently the key 3D fluorescent imaging technique used in bioscience. All underlying principles of excitation and emission of fluorescent light apply to confocal microscopy, with the major difference being the placement of a pinhole at the exact location of the relayed focal point, as shown in Figure 2.

Within a confocal microscope, the laser light is first reflected by a dichroic mirror (DM), which allows light within a certain wavelength band to be reflected and others to be transmitted before

being focused onto a point within the sample using an objective lens. The emitted fluorescent light is collected in the same pathway before passing through the dichroic mirror and forming a conjugated image plane. The pinhole aperture ensures that only fluorescent light coming from the confocal (conjugated) point where the laser is focused reaches the photon multiplier tube[9,14].

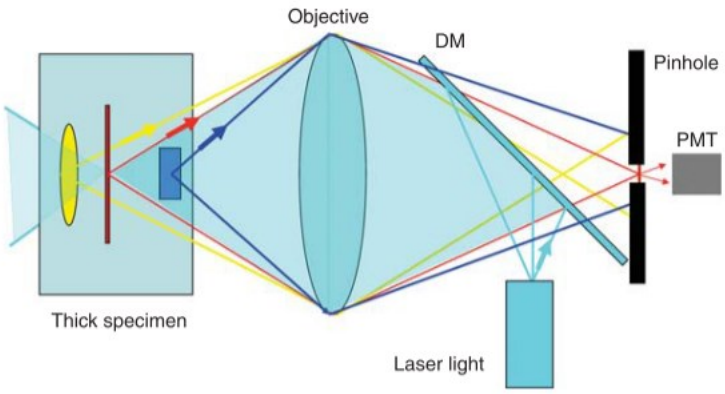

Figure 2 Working principle of a confocal microscope. A pinhole aperture is placed at the focused image plane to reject out of focus light. DM: dichroic mirror; PMT: photon multiplier tube. Image is reproduced with permission from Sanderson et al.[14]

There have been numerous advances in confocal microscopy over the years to improve its performance. Laser scanning confocal microscopy (LSCM) utilizes a dual-mirror galvo mirror that allows fast point-to-point scanning within the same z-plane. SDCM allows imaging of multiple points within the same focal plane at once by introducing an array of micro lenses. While this method significantly enhances the temporal resolution of the system, it sacrifices the achievable imaging depth[9]. Furthermore, pulsed infrared laser is incorporated as the light source in 2-photon confocal microscopy, which enables the system to outperform LSCM when imaging large samples ($>100\mu m$).

However, low temporal resolution of conventional confocal microscopy severely limits its However, the low temporal resolution of conventional confocal microscopy severely limits its capability to probe the dynamics of fast biological processes. As a result, another variation named scanning disk confocal microscopy was invented. To image multiple points within the surface, thousands of micro lenses are mounted on a spinning wheel together with a secondary wheel with pinholes in the same pattern. Thus, an array of focused laser spots can be projected onto the sample.

By synchronizing the frame rate of the camera and the rotation speed of the lens wheel, the entire image can then be reconstructed.

In addition to the much higher image throughput compared to LSCM, spinning disk confocal microscopy also results in much lower photobleaching. During the imaging session, LSCM scans each point once using a high power laser, while SDCM scans each point multiple times with low power laser created from the array of micro lenses. It has been found that the photobleaching curve of a fluorophore exhibits nonlinear behavior and low power excitation over a long time results in less photobleaching.

However, the crosstalk phenomenon caused by using a pinhole array significantly limits SDCM's ability to probe deep inside tissues. As the pinhole array is densely positioned, fluorescent light emitted from out-of-focus points can pass through the neighboring pinholes, contributing to background noise. This problem becomes more severe as the imaging depth increases and is difficult to avoid due to the nature of the pinhole array.

Despite the tremendous amount of effort dedicated to creating better confocal microscopes, there are several underlying limitations that restrict their usage and further development. First, the illumination mechanism of confocal microscopy unavoidably creates two cone-shaped unwanted illuminated volumes above and below the focal point. This property not only leads to unnecessary photobleaching but also generates a significant amount of light-matter interaction that degrades the quality of images[8,9]. Therefore, images generated using a confocal microscope heavily rely on computationally heavy 3D deconvolution to eliminate artifacts, and the system can hardly handle samples that are prone to photobleaching. Furthermore, the mechanism of point scanning constrains the volumetric imaging throughput of confocal microscopy. The integration time per pixel during the acquisition is lowered as the point scanning rate increases. Given the volumetric imaging speed needed to understand the dynamics of live samples, the required sampling rate has exceeded the capability of the electronic devices[8].

2.3. Dual Objective Light-Sheet Microscopy

To address the issues of high photobleaching and low volumetric image acquisition speed associated with confocal microscopy, dual-objective light-sheet microscopy was developed for 3D

imaging of large samples. The underlying principle of a light-sheet microscope is to generate a thin sheet of light $(0.5\sim4\mu m)$[8] that selectively illuminates the entire plane of interest. The formation of the light sheet is accomplished using an objective lens with the detection objective placed orthogonally, as shown in Figure 3. The generated light sheet can be characterized by its Rayleigh length, which is the distance from the waist of the light sheet to where the thickness doubles. Objectives with a high NA can produce an extremely thin light sheet at the waist but suffer from a short Rayleigh length, while a low NA objective can achieve the opposite[8,9]. With a thin light sheet at the waist, better optical sectioning can be performed, while the Rayleigh length dictates the maximum field of view.

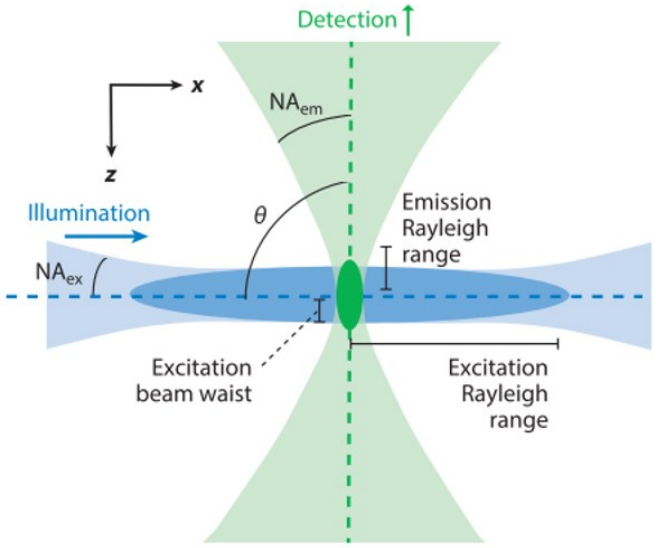

Figure 3 Working principle of a two-objective light sheet microscope where the detection objective is placed orthogonally with respect to illumination light sheet. Image is reproduced with permission from Hillman et al.[8]

The scanning of a two-objective light-sheet microscope is usually achieved by moving the entire sample through the light sheet so that both the illumination and detection objectives can remain stationary[9]. However, stage scanning often results in a coarse scanning step, and the vibrations induced by the movement may also be undesirable for live imaging applications. Thus, some designs incorporate a galvo mirror at the illumination objective for scanning the light sheet, and a piezo stage at the detection objective for high-speed repositioning[22].

Currently, multiple designs of two-objective light-sheet microscopes have been made completely open source, with an active community established[10,23]. As a result, the knowledge barrier to home-build a state-of-the-art two-objective light-sheet microscope with half or even less cost compared to commercial models has been significantly reduced. However, the conflict between the positioning of biological samples and the physical setup has become a major limitation of two-objective light-sheet microscopy. Considering the extremely short working distance of the objectives, the spacing between orthogonally arranged dual objectives can be tight. As a result, a specialized sample holder tube is often required, making the imaging of arrays of samples challenging[9].

2.4. Single Objective Light-Sheet Microscopy

Given the limitations of mounting options and usability, single-objective light-sheet microscopy was developed to provide a more user-friendly setup. Traditional dual-objective light-sheet microscopy requires the illumination plane and the detection objective to be strictly orthogonal to each other to avoid spherical aberration. However, to achieve simultaneous planar illumination and detection using the same objective, a tilted illumination had to be utilized. As described in section 2.4.1, an objective designed to satisfy the Sine condition can only ensure aberration-free imaging of the orthogonal-aligned, in-focused plane. When looking at a tilted imaging plane, the naturally fulfilled aberration-free imaging condition can no longer be satisfied[11,12,24–26]. The physics behind spherical aberration and the perfect imaging system will be further reviewed.

The idea of tilted illumination can be traced back to the design of Total Internal Reflection Fluorescence (TIRF) microscopy for 2D imaging. In TIRF microscopy, a laser beam is inputted from the very edge of the back focal plane of the objective to selectively illuminate the 2D surface in contact with the glass slide and avoid background noise. This results in a highly inclined illumination pathway. When the critical incline angle is reached, combined with the high refractive index difference between the glass slide and immersion medium, the laser beam is totally reflected within the objective. However, an evanescent wave is created due to the electromagnetic field of the laser, thus exciting fluorophores at the very surface in contact with the glass slide ($100\sim200nm$)[9,27,28]. Although TIRF microscopy still uses an orthogonal imaging plane for 2D

imaging purposes, the idea of utilizing a tilted illumination laser beam formed at the edge of the objective was created.

Building on top of the TIRF microscope, a 3D fluorescence microscopy technique was developed by Kumiko et al.[25] named Highly Inclined and Laminated Optical (HILO) microscopy. In this design, a thin light sheet is inputted from the edge of the back focal plane of the objective, forming a highly tilted imaging plane. However, the inclined angle is specifically chosen to be smaller than the critical angle so that the sample is directly illuminated by the sheet of laser instead of the evanescent wave. As a result, 3D imaging at a maximum depth of around 20μm can be achieved[25]. However, spherical aberration generated due to the inclined imaging plane cannot be corrected simply by tilting the camera[11,24]. Thus, HILO microscopy suffers from a very limited field of view and can only resolve the light sheet at its center, where it can be approximated as an orthogonal imaging plane.

To optically correct the spherical aberration without relying on approximation, Oblique Plane Illumination Microscopy (OPM) was developed[11]. Based on the idea that a perfect 3D imaging space could be relayed and reimaged through a remote refocusing system, OPM achieved a much deeper imaging depth and wider field of view by using a medium-inclined light sheet and a tilted remote refocusing system. On the other hand, the major drawback of a tilted-aligned remote refocusing system is the loss of NA. Although there are still no precise models to calculate the loss of NA, it is estimated that only 30% of the primary objective's NA can be preserved[13]. Furthermore, the stage scanning method provides poor scanning step resolution and can introduce disturbances during live imaging. Finally, the highly strict selection of optical components within the remote refocusing system leaves no room for magnification adjustment.

Recently, Swept Confocally Aligned Planar Excitation (SCAPE 2.0) Microscopy was developed by Voleti et al.[13], further extending the capabilities of OPM. By incorporating a galvo mirror traditionally used in scanning confocal microscopy, high-speed volumetric imaging acquisition can be achieved optically with simple control algorithms. This not only provides much finer scanning step resolution but also prevents sample disturbances due to vibrations and acceleration during stage movement. Furthermore, a commercial zoom lens was utilized outside the remote refocusing system, providing the ability to adjust magnification for different imaging demands.

2.4.1. Perfect Imaging System and Remote-Refocus System

Described by Maxwell in 1858[29], a perfect imaging system is one that can recreate the image of any point within a real 3D space by forcing all rays emitting from that point to reconverge at a single point within the imaging space[12]. To achieve this, the magnification between the real point and its image must be equal to $M = \frac{n_1}{n_2}$, where n_1 and n_2 are the refractive index of immersion medium of objective 1 and 2. The replica can then be reimagined using a tertiary objective without the concern of spherical aberration, and the primary objective can also be kept stationary throughout the imaging session. In the case of OPM, a perfect imaginary replica of the tilted imaging plane was created through a remote refocusing system, as shown in Figure 4. A magnification of 1.33X was ensured between IP2 and IP1, with water chosen as the immersion medium. Afterwards, a tertiary objective placed orthogonally to the replica was used in the same manner as a two-objective light sheet microscope. Thus, OPM was able to resolve constraints regarding physical spacing while optically removing spherical aberration induced by the tilted imaging plane.

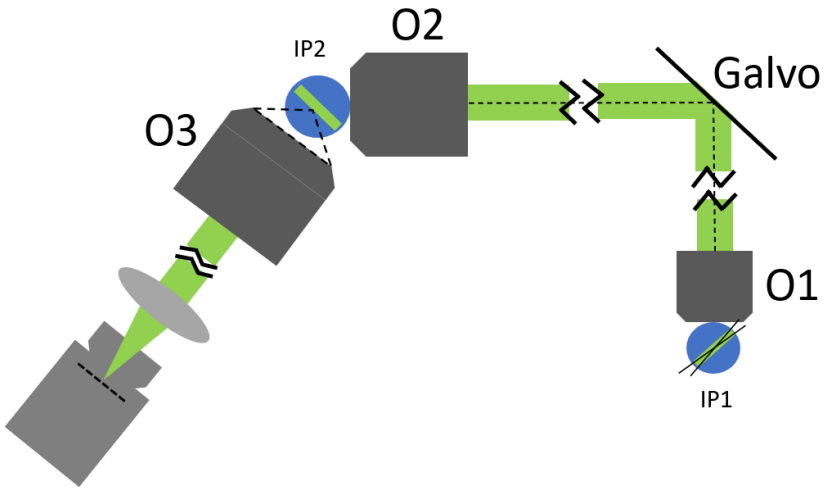

Figure 4 Simplified layout showing the real inclined imaging plane IP1 being perfectly replicated as an imaginary imaging plane IP2 using two objectives O1 and O2. A tertiary objective O3 was then placed orthogonally to IP2 for reimaging while avoiding spherical aberration

At the same time, one can see that the magnification required for a perfect 3D imaging system is extremely strict. Given that the refractive index of commonly used immersion medium in

microscopy ranges from 1 to 1.5, achieving high magnification in a microscope is theoretically never possible. To grossly magnify the biological object of interest, a departure from the perfect imaging system was used in virtually all objective designs. As shown in Figure 5b, an imaging system that satisfies the Sine condition allows uniform magnification of all points lying on the same plane perpendicular to the objective, while points outside the focusing plane are more axially magnified[12].

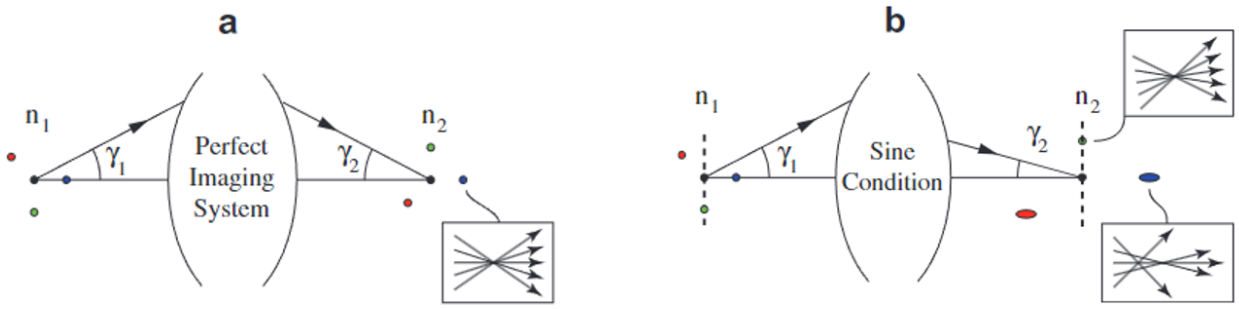

Figure 5 Difference between a) perfect imaging system; b) imaging system satisfies Sine condition. n_x, refractive index of objective x. γ_x, collection or converging angle of object x. Image is adapted with permission from Botcherby et. al[12]

2.4.2. 4f imaging system

The 4f imaging system is a fundamental and crucial technique used for image relay purposes. As shown in Figure 6, a collimated imaging space is formed between the lens pair when the object is precisely placed at the focal point of the collector lens. Traditionally, this collimated imaging space is treated as an infinite space, as each ray travels parallelly throughout the entire space, and the image can be perfectly restored at the focal plane of the detector lens. However, this assumption is only valid for a conventional image plane that lies perpendicular to the optical axis. When a tilted image plane is introduced, the phase profile of axially displaced points will be degraded by the additional curvature introduced by non-4f aligned lens pairs[12]. It should also be noted that it is common for a lens system (e.g., objective lens) to have a negative back focal plane, which means that an incoming collimated beam will be focused on a position within the system[30,31]. Extra care

needs to be taken when setting up a 4f system with such lenses, and a step-by-step protocol will be detailed in 3.1.2.

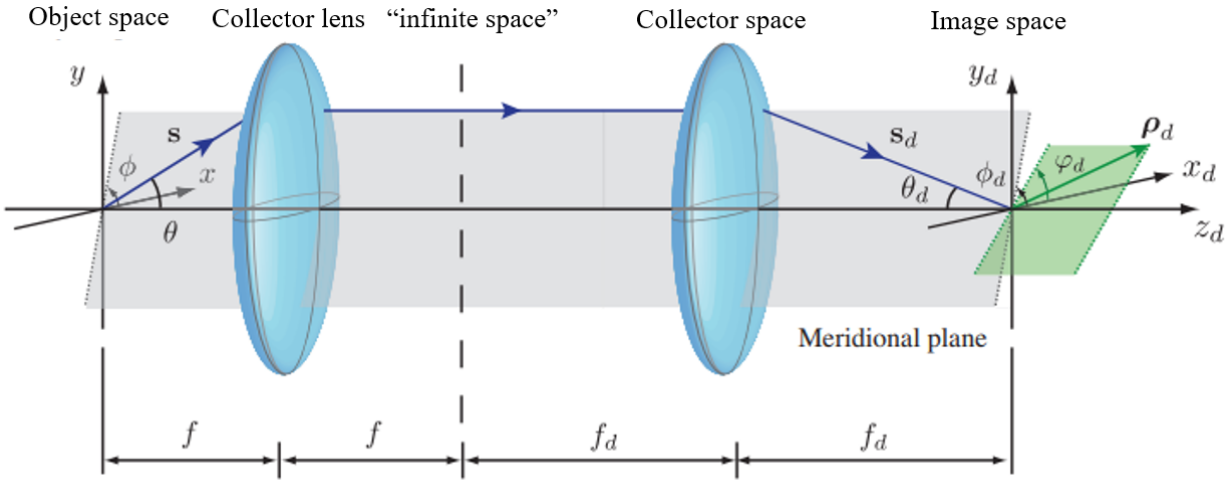

Figure 6 Illustration of a 4f system. Image is reproduced with permission from Foreman et al.[32]

2.5. Midbrain organoids and quality control challenges

Brain organoids are 3D neural tissue models derived from induced pluripotent stem cells (iPSCs), which have been widely used in the studies of neural development and disease processes[2–4]. The capability of self-organization and recreation of realistic human embryonic development processes distinguishes brain organoids from other types of in-vitro models, making them an emerging tool to facilitate the understanding of neurological diseases[2,5,33]. Furthermore, the use of brain organoids also presents fewer concerns regarding ethics and logistics[34]. Among different types of brain organoids that capture aspects of varied regions within the brain, the development of midbrain organoids containing functional dopaminergic neurons is of specific interest due to its relevance to Parkinson's disease[35]. However, due to the complex nature of stem cell development and differentiation, heterogeneous brain organoids are often found during mass production. The development of non-specific organoids presents significant economic and logistic challenges due to the expensive reagents used to facilitate the slow growth and differentiation of stem cells. One important marker used to determine the physiological properties of midbrain organoids is a structure called rosette. The presence of neural progenitor cells, including dopaminergic progenitors, at the center of rosettes can be used as confirmation of properly developed midbrain

organoids[35]. Traditionally, quality control of midbrain organoids during early development stages requires either cryosectioning or the use of tissue-clearing reagents. While cryosectioning provides unbeatable image quality, the delicate rosette can easily be damaged during the process. On the other hand, tissue clearing based on refractive index matching can preserve brain organoids while enhancing the capability to probe their 3D structures. By removing lipids and replacing intracellular fluids with a solution with a similar refractive index to proteins[6,7,36], dense tissue samples can appear transparent, making deep imaging within dense and large brain organoids possible. However, the time-consuming processes for tissue clearing (up to 2 weeks[6,7]) have also become the bottleneck for applications that require rapid generation of results, such as quality control.

3. Material and Methods

3.1. Microscope Assembly

The overall setup of the microscope is shown in Figure 7 with laser been represented by blue and fluorescent light been represented by green. The overall setup is further divided into 4 subsections for details of alignment procedures. In addition, equipment used for assembling will be listed at the end of each section. It should be noticed that all optics were setup on a secondary breadboard that was elevated around 6inch higher than the optical table. The illumination laser was setup on a separate breadboard that is elevated around 1.5inch higher than the first one. This is done so that it provides enough space in z-direction for the alignment of optics and electronics could also been housed under elevated breadboard to save space. In addition, a bright-field imaging system was added in section 1 by using a removable turning mirror 2, S3, T4 and camera 2. This is done so that it provides the system a much easier way to locate the sample and the region of interest prior to the 3D scanning.

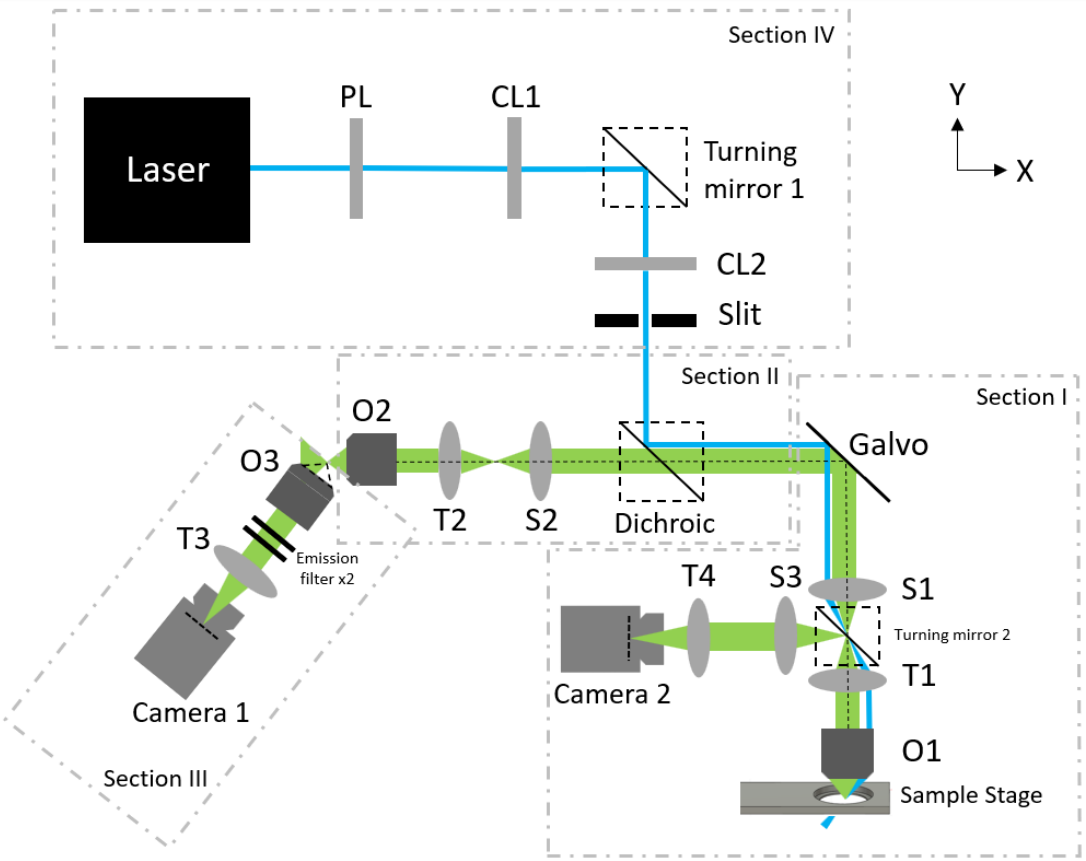

Figure 7 Overall setup of the microscope with subsections

Apart from the equipment and tools used in individual sections, several other equipment was used throughout the entire process for the calibration and mounting purpose. Cage system is widely used within the system to facilitate easier mounting and alignment. Both 30mm and 60mm cage system are used due to the need of lens in different size. As a result, generic naming will be used regarding cage system in subsections and the amount used will be detailed in tables. For calibration purpose, a shear plate compatible with beam size from 1-3mm (Thorlabs, SI035) were used to test collimation of beams. Another 4.5mW collimated laser module at 532nm with 3.5mm round beam size (Thorlabs, CPS532) was used to assist the alignment. The collimated laser module was fitted into the 30mm cage system by a SM1-threaded adaptor (Thorlabs, AD11F) and mounted onto a quick-release cage plate (Thorlabs, CP44F). In addition, both post-mountable and cage system iris diaphragms (Thorlabs, ID25 and CP20D) were used for lens positioning. Finally, laser viewing cards (Thorlabs, VRC1 and VRC2) were used to visualize the laser beam while eliminating its potential harm to eyes.

Before any part of the microscope was assembled, a 30×48inch optical table with 4inch thick breadboard (Newport, VIS3048-PG4-325A) was floated using compressed nitrogen. The flatness of the surface was first checked by making sure the bubble leveler on each stand of the optical table was centered. After that, illumination laser (HUBNER Photonics) was used, and the height of the laser beam was measured over a long distance for verification. It is important to use the minimal laser power available (~1mW) during the flatness verification and a laser safety glass (ex. Thorlabs, LG14) should be used.

Finally, magnification at $M = \frac{n_1}{n_2}$ between O1 and O2 must be satisfied for remote refocusing purpose, according to section 2.4.1. Given that a water-dipping and air objective were used as O1 and O2 respectively, $M = 1.33$ is needed. Considered the physical spacing and commercial availability, the choice of individual lens and magnification calculation is shown below:

$$M = M_{O1} \times \frac{F_{T1}}{BFL_{O1}} \times \frac{F_{S2}}{F_{S1}} \times \frac{BFL_{O2}}{F_{T2}} \times \frac{1}{M_{O2}}$$

$$= 20 \times \frac{150mm}{180mm} \times \frac{60mm}{75mm} \times \frac{200mm}{100mm} \times \frac{1}{20} = 1.33$$

Table 2 General items used throughout all alignment processes

Item description	**Part number (Vendor)**
Shear plate (1-3mm beam diameter)	SI035(Thorlabs)
Collimated laser module, 532nm	CPS532(Thorlabs)
SM1-threaded adaptor	AD11F(Thorlabs)
Quick-release cage plate	CP44F(Thorlabs)
Post-mountable Iris diaphragms	ID25(Thorlabs)
30mm cage system Iris diaphragms	CP20D(Thorlabs)
Laser viewing cards (UV/Vis and Vis/NIR)	VRC1, VRC2(Thorlabs)
Laser safety glass	LG14(Thorlabs)
Illumination laser, 488nm	C-flex Series(HUBNER Photonics)
30×48inch optical table	VIS3048-PG4-325A(Newport)

3.1.1. Module I: scanning and de-scanning

The general layout and real setup of module 1 is shown in Figure 8 and it serves for 4 functions within the microscope: light-sheet scanning, fluorescent de-scanning, aligning laser enlargement and bright-field imaging. An aligning laser enlargement module is used so that its small laser spot could eventually overfill the back aperture of O2 in module 2 for easier alignment. Regular setup where aligning laser replaces O1 during the alignment would results in 0.83X demagnification of laser spot, compared with 4.16X magnification with enlargement module used.

For a perfect parallel light-sheet translation during the scanning, the laser spot on galvo needs to be relayed on to the back focal plane within O1. Thus, a 4-f system needs to be formed between galvo mirror and O1. In addition, a well-aligned 4-f system also ensures proper de-scanning of the image. Otherwise, image drifting will be observed on the camera. Finally, it should be noted that the collimation and divergence of the light-sheet will be different depends on angle of viewing as illustrated in Figure 9.

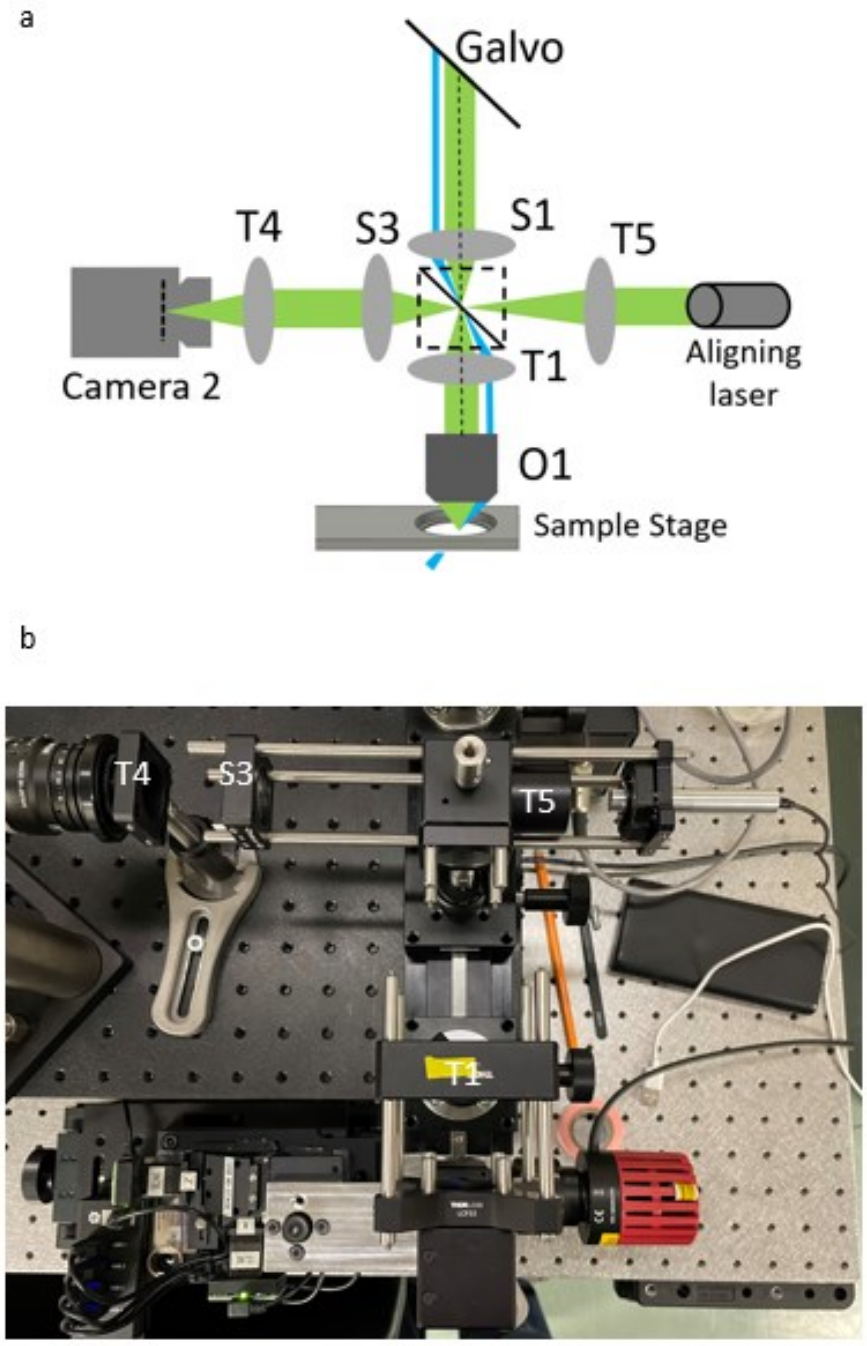

Figure 8 a) Schematic layout of module 1; b) Real setup of module 1

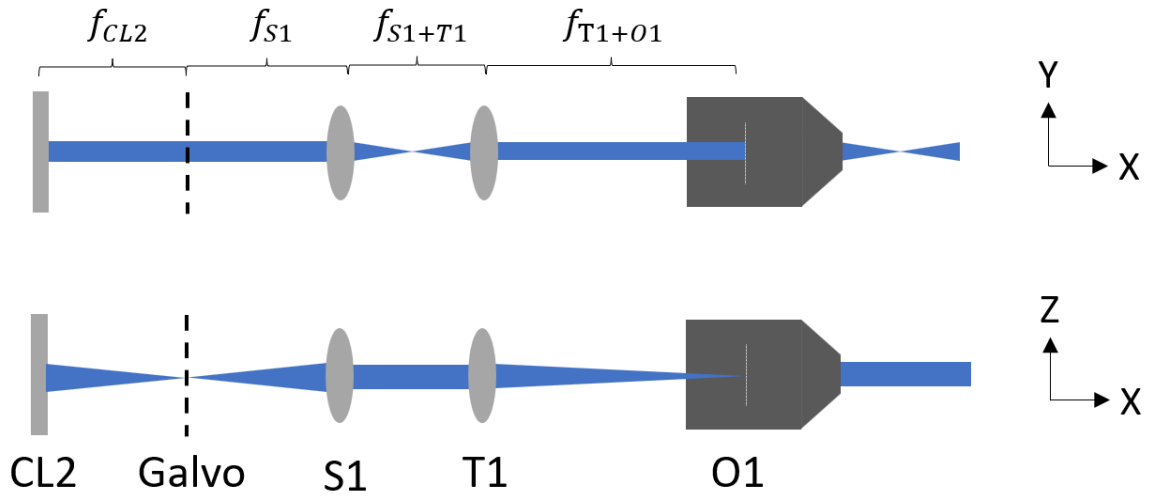

Figure 9 Collimation and divergence of light-sheet viewing from different axis

For major components used for light-sheet microscope, one 12inch travel rack and 3 pinion stages (Edmund Optics, 59-334 and 59-331) are required and a 1D large beam galvo-mirror (Thorlabs, GVS011) is needed to avoid image clipping. Both S1 and T1 are mounted using 60mm cage plate, ½'' post and post holder. The high numerical aperture water immersion objective O1 (Olympus, XLUMPLFLN20XW) was connected with T1 through a 30mm-60mm cage adaptor (Thorlabs, LCP33). After that, a 30mm cage compatible turning cube (Thorlabs, CCM-G01) was used to turn the scanning light-sheet downwards for easier water immersion during the imaging process.

For major components used for bright-field imaging system, a rectangular mirror (Thorlabs, FM03R) is housed using a 30mm cage cube (Thorlabs, CM1-DCH). The cage cube was mounted upside down so that its base where the mirror is attached could be removed freely to enable or disable the function of bright-field imaging. A 75mm achromatic doublets (Thorlabs, AC254-075-A) was mounted using lens tube (S3 in Figure 8a) and a 35mm machine vision camera lens (Thorlabs, MVL35M1) was used as T4. As the bright-field imaging only serves for easier sample location, a light weight, compact scientific camera (Thorlabs, CS165MU) was used. In addition, two more mounting adaptors (Thorlabs, SM1A57; Edmund Optics, 12484) were used to fit the camera into a 30mm cage plate. Finally, a mounted LED (Thorlabs, M450LP2) attached with collimator (Thorlabs, SM1U25A) was used as the light source for bright-field microscope.

For the setup of elevated breadboard, 2 separate board with size 12×18inch and 24×24inch (Thorlabs, MB1218 and MB2424) were used for illumination module and the rest of microscope system. One tapped hole at each corner of the breadboard was machined into a clearance hole so it can be aligned with the optical table using 1.5'' posts.

Setting up reference points:

1. Mount both galvo mirror and S1 using ½'' post and post mount, both their x-y location and height does not need to be precise
2. Turn on illumination laser and set it to the minimal power
3. Bring the galvo mirror in front of the laser. Adjust the height of ½'' post to make sure laser centers on galvo mirror's z-axis. Depends on the manufacturer of the galvo mirror, its rotation center may not be the same as its mounting center. A customized plate may be required to fix it.
4. Tighten the set screw and use a post collar on galvo mirror's post to mark and fix its height
5. Mount the post holder of S1 onto the front most manual stage on the translation rack
6. Use 2 sets of cage rod and a 30-60mm cage adaptor to connect an iris to the back of S1
7. Bring the entire rack with S1 attached in front of the laser. Adjust both position of the rack and height of ½'' post to make sure laser passing through the iris hole after S1
8. Tighten the set screw and use a post collar on S1's post to mark and fix its height. This will be the primary height reference for the rest of microscope system

Setting up O1 objective:

1. Thread O1 objective onto a cubic turning mirror
2. Thread in a set of short cage rod onto the turning mirror
3. Mount T1 using a 60mm cage plate and use 1 set of cage rod to connect it with a 30-60mm cage adaptor
4. Place a set of long enough cage rod into aligning laser's cage plate
5. Connect the aligning laser with turning cube so that aligning laser and front-end of the objective are face-to-face

6. Connect turning mirror with cage adaptor. Making sure cage rod slides all the way to the end before tightening
7. Turn on the aligning laser, a spherical laser spot should be observed behind the T1
8. Slightly loosen the set screw on the outer holes of 30-60mm cage adaptor to slide the cage adaptor back and forth
9. Place the shear plate in the center of the laser spot. Keep adjusting the position of the cage adaptor until the shearing pattern is parallel to the reference line
10. Tighten the set screw on cage adaptor and remove the aligning laser by unscrewing the rod connected in step 5. The relayed system between T1 and O1 is now formed. The real setup is shown in Figure 10

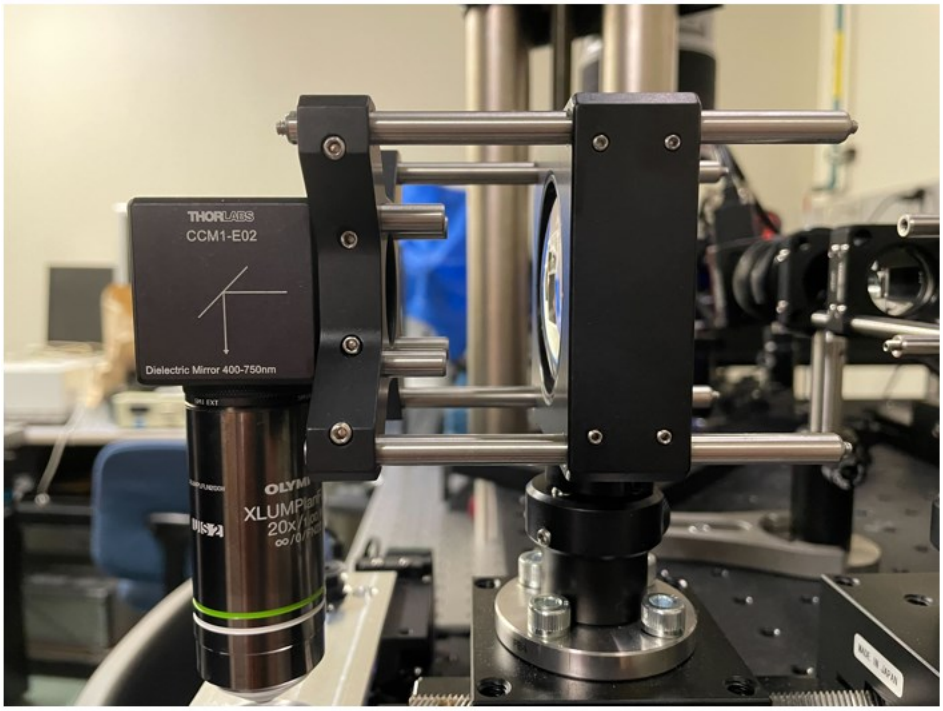

Figure 10 Connection between O1 and T1for easier tuning of relay system

Setting up 4f system:

1. Mount the translation rack on the right side of the breadboard, making sure its back end (oppose to the side with S1 mounted) is aligned with the edge of breadboard
2. Insert aligning laser in in cage adaptor connected to S1.

3. Place 2 post mountable iris in front of S1, making sure they are not too close with each other. Use the aligning laser coming out of S1 to adjust the height of iris
4. Once the height of irises is fixed, loosen the set screw on S1 and rotate it until the aligning laser passing through the center of both iris
5. Remove aligning laser from S1 and use it to replace O1 with its turning mirror
6. Mount T1 on the back most stage on the translation rack, leaving the middle one for bright-field imaging system
7. Turn on the aligning laser and adjust both the height and rotation of T1 until the light coming after S1 passing through the center of both iris.
8. Tighten the set screw and use a post collar to fix the height of T1
9. Remove irises and move the aligning laser back to the cage adaptor on S1
10. Mount galvo mirror at top right corner of the breadboard. Making sure to use the closest hole available in front of the S1. By using tapped holes available on breadboard, the center of galvo mirror and S1 should be auto aligned
11. Using the knob on the translation stage to adjust the position of S1 until the laser spot is focused on the galvo mirror. Use the set screw on the stage to fix its position
12. Move the aligning laser to the cage adaptor on T1 and adjust its position using the knob
13. Place the shear plate in the center of laser reflected by galvo mirror and adjust the position of T1 until the shear pattern is parallel to the reference line
14. Remove the aligning laser and put back O1 objective with its turning mirror. The 4f system in module 1 is completed

Setting up bright-field imaging system and laser enlargement:

1. Ensure all above alignment procedures are complete and place the aligning laser on T1 by replacing O1 objectives with its turning mirror
2. Place 2 post mounted iris after galvo mirror, adjust their height to the same level of reflected beam from galvo mirror
3. Use MATLAB to control the angle of galvo mirror (details can be found in 3.2.3) until the laser beam passes the center of both iris

4. Thread T4 onto the camera. Then use M35.5-T and T-SM1 mount adaptor to connect front-end of T4 onto a 30mm cage plate
5. Use 2 separate lens tube to mount both S3 and T5. Then mount S3 onto a 30mm cage plate and T5 directly onto the cage cube. Opposite side of the cage cube should be used
6. Remove aligning laser from T1, then use 2 sets of cage rods to mount camera, S3 and aligning laser onto the cage tube. The positioning does not need to be precise
7. Mount the cage cube (with mirror attached to the base) upside down onto the middle stage on the track and turn on the aligning laser
8. Adjust the rotation and height of the cage cube mount until the laser passes the center of both iris setup in step 2
9. Tighten the mount of cage cube and adjust the location of the manual stage using the knob until the laser reflected from galvo is collimated (use shear plate for confirmation)
10. Switch the aligning laser back onto T1 and adjust the position of S3 until the light coming out from it is collimated
11. Put the aligning laser back onto the cage cube and place back the O1 objective. Both bright-field imaging system and laser enlargement is now set up. The bright-field imaging system can be turned on or off by simply keep or remove the mirror in the cage cube

Table 3 Part list for module 1

Optical Part	**Part description**	**Part number (Vendor)**
Galvo mirror	1D large beam scanner	GVS011 (Thorlabs)
S1	75mm achromat	49-292 (Edmund Optics)
T1	150mm achromat	49-285 (Edmund Optics)
O1	XLUMPLFLN 20x/1.0NA W	XLUMPLFLN20XW (Olympus)
T5	30mm mounted achromatic doublet	AC254-030-A-ML (Thorlabs)
S3	75mm achromatic doublet	AC254-075-A (Thorlabs)
T4	35 mm EFL, f/1.4	MVL35M1 (Thorlabs)
Removable mirror	25×36mm visible cold mirror	FM03R (Thorlabs)
Bright-field camera	1.6MP monochrome CMOS camera	CS165MU (Thorlabs)

Mounting part	Part description	Part number (Vendor)
Cage Cube	30mm cage cube for rectangular Optics	CM1-DCH (Thorlabs)
Travel track	12" pinion track	59-334 (Edmund Optics)
Manual track stage ×3	1 Knob stage	59-331 (Edmund Optics)
60mm cage plate ×2	SM2 threaded, 0.9" thick	LCP34T (Thorlabs)
30-60mm cage adaptor ×2	0.5" thick	LCP33 (Thorlabs)
Turning mirror	30mm cage turning mirror	CCMG01 (Thorlabs)
Lens tube ×2	1" lens tube, SM1 threaded	SM1L10 (Thorlabs)
30mm cage plate ×2	0.35" thick, SM1 threaded	CP33 (Thorlabs)
M35.5 to T mount adaptor	M35.5 external and T mount internal	12484 (Edmund Optics)
T mount to SM1 adaptor	T mount external and SM1 internal	SM1A57 (Thorlabs)
1.5" post ×2	1/2" optical post	TR1.5 (Thorlabs)
0.75" post ×2	1/2" optical post	TR075 (Thorlabs)
Cage rod set ×5	Length varied depends actual need	(Thorlabs)
1" post holder ×2	1/2" post holder	PH1 (Thorlabs)
1.5" post holder ×2	1/2" post holder	PH1.5 (Thorlabs)
Post collar ×3	Thin slip-on post collar	R2T (Thorlabs)

3.1.2. Module II: magnification conditioning

The general layout of module 2 is shown in Figure 11 and it mainly serves for image relay and magnification adjustment. As the perfect imaging system requires a magnification of 1.33 between the focal point of O1 and O2, an extra pair of relay lens is need for such magnification adjustment purpose. The major alignment goal for module 2 is to form a 4-f system which follows similar procedures as mentioned in module 1.

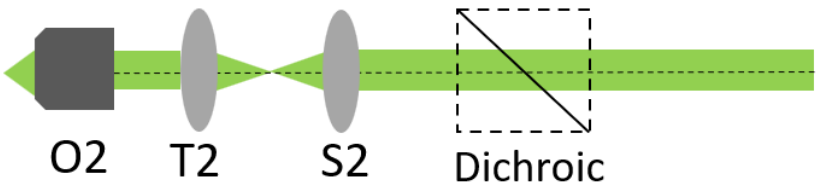

Figure 11 General layout of Module 2

For major components used for module 2, one 12'' travel track with 3 one-knob stages from Edmund Optics were used. A 30mm cage cube for rectangular optics from Thorlabs was used to house dichroic mirrors (Thorlabs, DMLP505R and DMLP605R) that matches the excitation and emission spectrum of the laser. A pair of 60mm and 100mm achromatic lens (Thorlabs, AC254-060-A and Edmund Optics, 49-284-INK) were used as S2 and T2. Finally, a 20X, high NA air objective (Nikon, CFI Plan Apo Lambda 20x/0.75 NA) were used as O2.

Alignment for module 2:

1. Mount the long travel rack onto the breadboard, the center of optics mount should be auto aligned with the center of galvo
2. Place 2 post mountable iris on the second and third one-knob stage. Adjust the voltage input to the galvo mirror using MATLAB until the reflected laser beam passes through the center of both iris

   *Note down the final value and it will be the reference voltage in the future
3. Check the collimation of reflected laser beam using shear plate. If it is not collimated, it would be an indication of poor alignment in module 1
4. Using a lens tube to mount S2 before threading it onto the dichroic cage cube
5. Threading a set of cage rod to dichroic cage cube on the side with S2 mounted. Then mount a 30mm cage cube onto the cage rod relatively close to S2. The position doesn't need to be precise. This will be referred as "S2-dichroic" in later steps
6. Unthread T5 in module 1, the laser beam should now focus onto the galvo mirror. After that, mount S2-dichroic using post on the first one-knob stage.
7. Adjust the height and rotation of S2-dichroic until the laser beam passes through the center of both iris
8. Using shear plate to check if the laser beam after S2-dichroic is collimated. Adjust the position of one-knob stage on the track until the laser is collimated.

   *The space between S2-dichroic is very limited, adjust the spacing between the 30mm cage plate and S2 in step 4 if needed

9. Remove the iris from the second stage and placed somewhere further along breadboard's tapped hole for later reference. Thread T5 back in module 1 and mount T2 using a 60mm cage plate
10. Mount T2 on the second one-knob stage. Adjust its height and rotation until the laser beam passes both irises. Using shear plate as reference and adjust the position of the stage until laser coming out of T2 is collimated
11. Remove both iris and aligning laser in module 1. Mount a cage compatible iris onto the position where aligning laser used to be.
12. Using a C-SM1 adaptor to thread O2 onto a 30mm cage plate. Using a set of cage rod to mount the aligning laser directly on the front side of the O2
13. Mount O2 onto the third one-knob stage using post. Then turn on the laser and adjust both height and rotation of O2 until the laser beam passes the center of iris in step 10
14. Unthread T5 and use the shear plate to check laser's collimation. Adjust the stage with O2 mounted until the laser coming after the iris is collimated
15. Remove the aligning laser from O2's mounting plate. Remove the iris from step 10 and place back the aligning laser. Do not thread back T5
16. Mount the iris on the back side of O2's plate. Turn on aligning laser and readjust the height and rotation of O2 until the laser beam coming through T2 passing the center of iris
17. Remove iris from O2 and thread back T5. Module 2 is now fully aligned as a 4f system. *The dichroic mirror can either be removed or inserted during the alignment as it does not affect the pathway of laser

Table 4 Part list for module 2

Optical Part	**Part description**	**Part number (Vendor)**
Dichroic mirror for GFP	505nm cut-on long-pass dichroic mirror	DMLP505R (Thorlabs)
Dichroic mirror for TRITC	605nm cut-on long-pass dichroic mirror	DMLP605R (Thorlabs)
S2	60mm achromat	AC254-060-A (Thorlabs)
T2	100mm achromat	49-284 (Edmund Optics)
O2	CFI Plan Apo Lambda 20x/0.75 NA	(Nikon)
Mounting part	**Part description**	**Part number (Vendor)**
Cage Cube	30mm cage cube for rectangular Optics	CM1-DCH (Thorlabs)

Travel track	12" pinion track	59-334 (Edmund Optics)
Manual track stage ×3	1 Knob stage	59-331 (Edmund Optics)
60mm cage plate	SM2 threaded, 0.9" thick	LCP34T (Thorlabs)
Lens tube	1" lens tube, SM1 threaded	SM1L10 (Thorlabs)
30mm cage plate ×2	0.35" thick, SM1 threaded	CP33 (Thorlabs)
C mount to SM1 adaptor	C mount internal to SM1 external	SM1A10 (Thorlabs)
1.5" post ×2	1/2" optical post	TR1.5 (Thorlabs)
0.75" post	1/2" optical post	TR075 (Thorlabs)
Cage rod set ×2	Length varied depends on actual need	(Thorlabs)
1" post holder	1/2" post holder	PH1 (Thorlabs)
1.5" post holder ×2	1/2" post holder	PH1.5 (Thorlabs)
Post collar ×3	Thin slip-on post collar	R2T (Thorlabs)

3.1.3. Module III: remote re-imaging

The general layout of module 3 is shown in Figure 12 and it mainly serves to reimage the aberration corrected but still tilted image plane onto the camera. It should be noticed that a right-angle turning mirror can be placed behind O3 if spacing was not sufficient for the linear layout of module 3. In addition, 2 identical emission filters were used in series as the reflection of light-sheet could not be fully blocked in some cases with only one single filter. The choice of O3 dictates the overall magnification range of the system. A commercial photography zoom lens was chosen over microscopy camera lens with fixed focal distance so that it gives some flexibility in adjustment of magnification. Furthermore, both T3 and camera were mounted vertically for easier alignment. As a result, another right-angle turning mirror was used after emission filters to direct the light upward. Finally, the assembly and alignment of module 3 is rather simply compared to other modules as it does not require a 4f system setup. However, the alignment between module 2 and module 3 is the most important and hardest part of the entire system. Detailed step by step procedure will be presented in section 3.1.5.

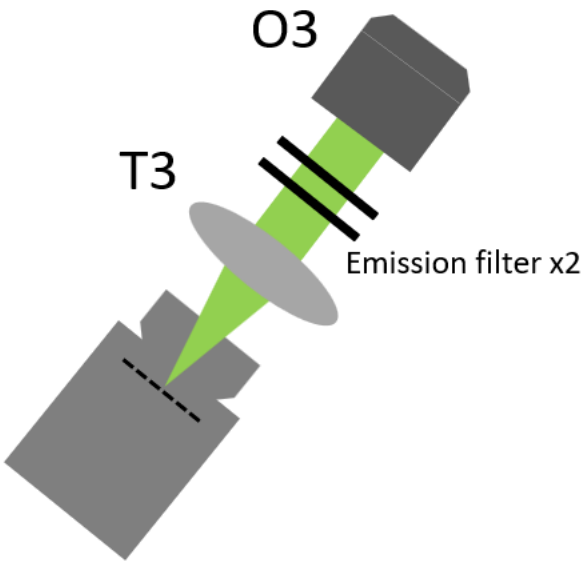

Figure 12 General layout of module 3

For major optical components used in module 3, a 20X, high NA dry objective (Edmund Optics, 58-373) was used. However, the choice of O3 is rather flexible and another 10X, high NA dry objective (Nikon, CFI Plan Apo Lambda 10x/0.45 NA) can also be used as an alternative. 2 sets of pre-mounted emission filters for GFP and TRITC (Thorlabs, MF525-39 and MF620-52) were used with 2 manual filter wheels (Thorlabs, CFW6). A commercial photography zoom lens (Canon, EF 70-200 f/2.8L IS III) was used as T3 for flexible magnification adjustment. Finally, a sCMOS camera (Andor Oxford instrument, Zyla 4.2+) was used to capture final images.

Alignment for module 3:

1. Using a C-SM1 adaptor to mount O3 onto a right-angle turning mirror cube. Then use a post, post holder, base adaptor and clamping fork to secure O3 onto a 4’’×6’’ breadboard
2. Using a set of cage rod to mount a cage compatible iris on the exiting side of the turning mirror cube

3. Turn on the aligning laser and place O3 head-to-head toward O2. The angle between O2 and O3 should be roughly 180° and the spacing should roughly be 15mm ($WD_{O2} + WD_{O3}$)
4. Adjust the height of O3 until the light from the backside of O3 passes through the center of iris. Tightly secure the side screw of post holder and use a post collar to further secure its height
5. Remove iris and mount 2 manual filter wheel in series on the exit side of the turning cube. It should be noticed that only bottom 2 cage rods should be used according to the instruction of the filter wheel
6. Slide in another 30mm cage plate with post after emission filters. Then mount a turning mirror onto the cage plate with top 2 cage rod threaded only
7. Machine the long travel vertical stage that it is securely connected to the tripod mount for T3
8. Thread an EOS-C mount adaptor onto T3 and carefully insert it into the vertically mounted tripod before connecting it to the camera. Firmly secure the tripod. The final setup of T3 and camera is shown in Figure 13

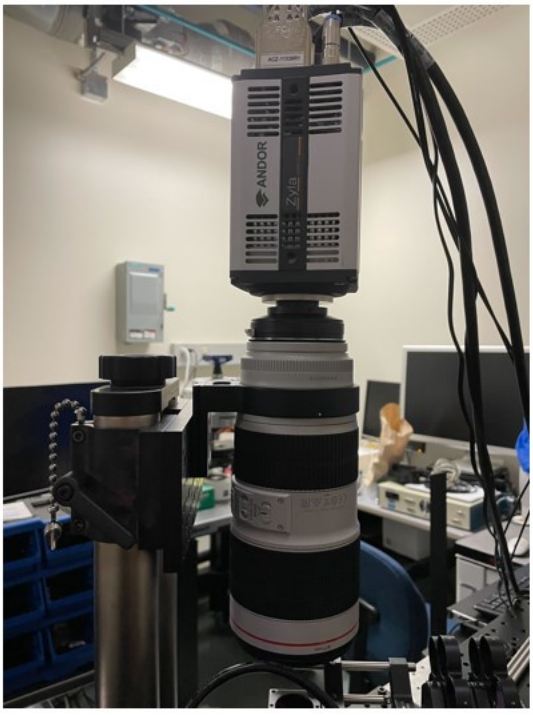

Figure 13 Vertically mounted camera with T3 using tripod and vertical translation stage

9. All components in module 3 is now set up. All components before T3 were mounted on one single breadboard and will be referred as “the breadboard plate” in section 3.1.5

Table 5 Part list for module 3

Optical Part	**Part description**	**Part number (Vendor)**
O3	EO HR 20x/0.60 NA	58-373 (Edmund Optics)
GFP emission filter ×2	CW=525, BW=39	MF525-39 (Thorlabs)
TRITC emission filter ×2	CW=620, BW=52	MF620-52 (Thorlabs)
T3	70-200mm, f/2.8 Zoom	EF 70-200 f/2.8L IS III (Canon)
Camera	sCMOS	Zyla 4.2+ (Andor Oxford Instruments)
Mounting	**Part description**	**Part number (Vendor)**
Breadboard	4"x6", tapped	MB4 (Thorlabs)
C mount to SM1 adaptor	C mount internal to SM1 external	SM1A10 (Thorlabs)
Turning mirror ×2	30mm cage turning mirror	CCMG01 (Thorlabs)
filter wheel ×2	30mm cage manual filter wheel	CFW6
EOS-C mount adaptor	C mount external, EOS internal	(Amazon)
Tripod	tripod for Canon 70-200 lens	(Amazon)
vertical translation stage	10" vertical travel	VAP10 (Thorlabs)
30mm cage plate	0.35" thick, SM1 threaded	CP33 (Thorlabs)
Cage rod set	Length varied depends on need	(Thorlabs)
1.5" post ×2	1/2" optical post	TR1.5 (Thorlabs)
1.5" post holder ×2	1/2" post holder	PH1.5 (Thorlabs)
Base adaptor ×2	1.25" pedestal base adaptor	BE1 (Thorlabs)
Table clamp ×2	1/4" 20 tapped	CL2 (Thorlabs)

3.1.4. Module IV: light sheet formation

The general layout of module 4 is shown in Figure 14 and it mainly serves for light sheet generation and conditioning. It should be noticed that an open space laser was used in the system, and it is suggested to consider a fiber laser if the wavelength and power is compatible. At the same time, a Powell lens was used to form the light sheet instead of the traditional cylindrical lens. The beam intensity profile of light sheet generated using Powell lens is flat top and provides better uniform

illumination compared to 2D gaussian intensity profile generated using a cylindrical lens. However, the irregular geometric nature of Powell lens poses challenges for mounting options. As a result, a customized mounting piece shown in Figure 15 was machined to house the Powell lens and adapt it into a 30mm cage system. It should be noticed that the mounting piece must be machined as "slide fit" instead of commonly used "press fit" to preserve the delicate optics. Finally, as the tilt angle is solely defined by the deviation between the light sheet pathway and optical center of galvo mirror, a manual or motorized high precision 2D stage should be used to facilitate the angle adjustment.

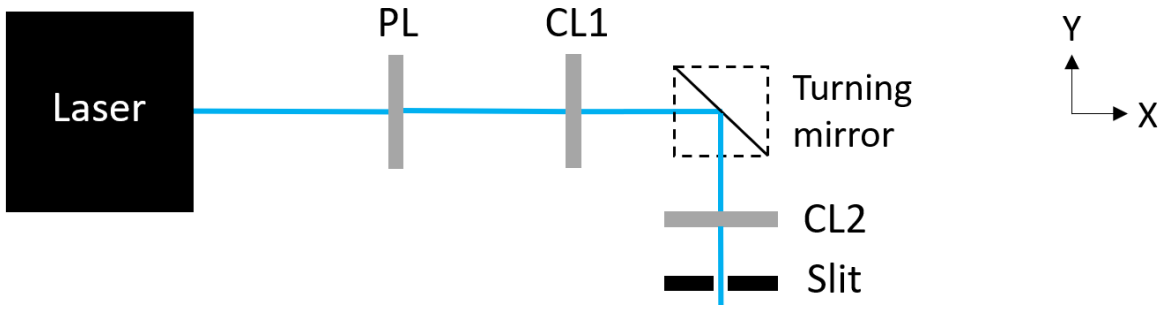

Figure 14 General layout of module 4

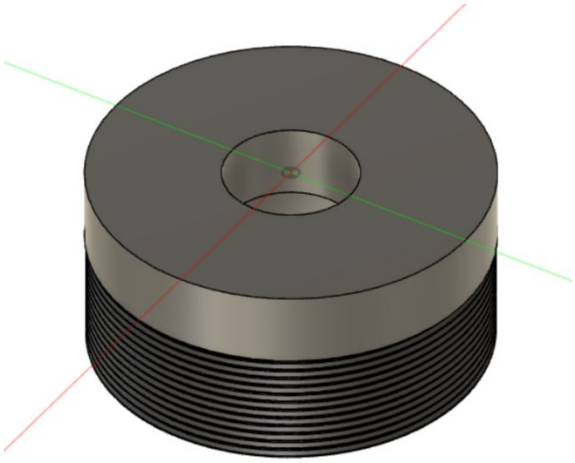

Figure 15 Customized and machined slide fit mounting adaptor for Powell lens

For major components used in module 4, an 8.9mm, 30° Powell lens designed for 0.8mm beam diameter (Laserline Optics, LOCP-8.9R30-1.0) was used to generate the light sheet. Afterwards, two cylindrical lenses with 50mm and 75mm focal distance were used as CL1 and CL2 (Thorlabs, LJ1695RM-A and LJ1703RM-A). It should be noticed that rotational cage plates (Thorlabs, CRM1T) were used instead of standard cage plates due to the rotational variant nature of Powell lens and cylindrical lenses. A turning cube compatible with 30mm cage system (CCM-G01) was also placed between CL1 and CL2 due to the physical layout of the system. After CL2, a manually adjustable slit compatible with 30mm cage system (VA100CP) was used for further conditioning of the light sheet. Finally, a manual XY translation stage (XYR1) was used to mount turning cube, CL2 and slit altogether which allows a fine adjustment of the tilt angle of light sheet.

Preliminary alignment for module 4:

1. Check if the output hole of system laser is aligned with the tapped hole on the breadboard.
2. Thread the machined Powell lens adaptor into a rotational 30mm cage plate and slide in the Powell lens
3. Mount the Powell lens and its rotational cage plate using post and post holder directly into a tapped hole on the breadboard
4. Turn on system's laser and adjust the height of mounting for Powell lens until a light sheet with uniform intensity distribution is formed
5. Tightly secure the Powell lens mount and use a set of cage rod to mount the slit at the back of Powell lens
6. Adjust the rotation angle of the Powell lens until a perfect vertical light sheet is formed
7. Check if the intensity of light sheet is still uniform. If not, repeat step 2 to 4 until both intensity is uniform and light sheet is vertical
8. Remove the slit but keep the cage rod. Put CL1 at the back of Powell lens and the slit after CL1
9. Adjust the rotation angle of CL1 until a perfect vertical light sheet passes through the slit. *There are two possible angles that gives the same results, but light sheet should be collimated after CL1. As a result, the rotation angle results in clear divergence should not be used

10. Adjust the spacing of CL1 and Powell lens until the light sheet is collimated
11. Remove the slit. Using cage rod and rotational cage plate to mount the turning cube, CL2 and slit altogether. This will be referred as “angle system” in future steps. It should be noted that the post and post holder should only be placed on the turning cube
12. Mount the angle system onto the XY translation stage and use two 30-60mm cage adaptor to ensure the angle system is well aligned with tapped holes on translation stage. Picture is shown in Figure 16

a b

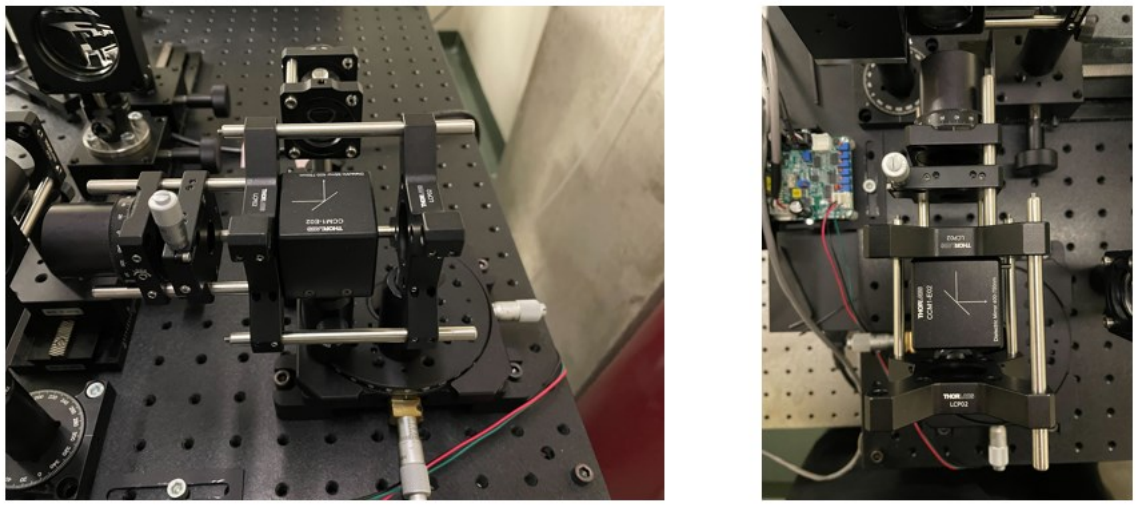

Figure 16 a) side view of the angle system; b) top view of the angle system

13. Mount the XY translation stage onto the breadboard so that the light sheet roughly hit the center of turning cube (in all X, Y and Z axis)
14. Adjust the rotation angle of CL2 until the light sheet is vertical and is collimated in x-axis while divergent in y-axis

    *x and y are used here to distinguish them from the axis used for entire module 4 The geometry of light sheet is shown in Figure 17

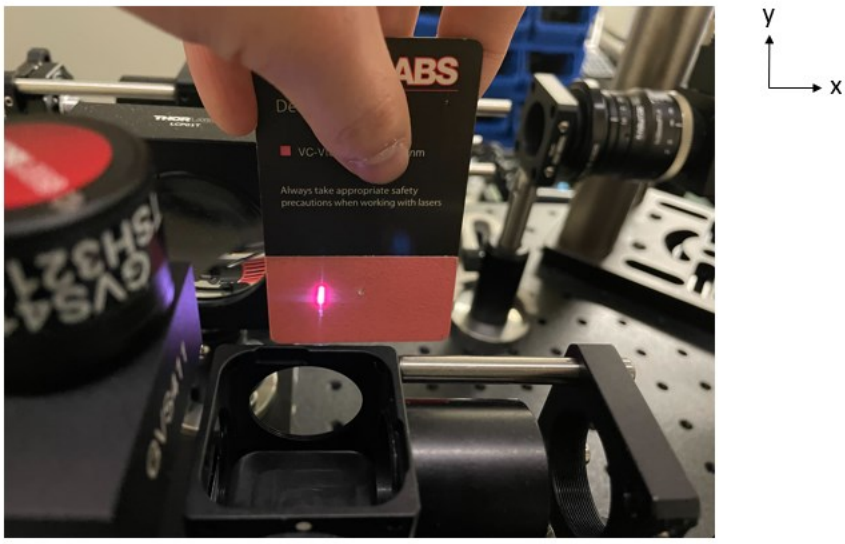

Figure 17 x-axis collimated and y-axis divergent light sheet

15. Adjust the translation stage in Y axis using the knob until the light sheet passes through the center of slit after CL2
16. Adjust the translation stage in X axis using the knob until the light sheet hits roughly the center of dichroic mirror in module 2
17. The preliminary alignment of module 4 is completed. The fine alignment of the spacing between CL2 and CL1, height of angle system and translation stage in X axis will be described in detailed in next part

Fine alignment of module 4:

1. Dissolve a small amount of fluorescein using 1ml of 70% ethanol
2. Dilute the fluorescein solution using PBS until the solution is transparent to bare eyes
3. Add 50ml of diluted fluorescein solution to a beaker for fine alignment
4. Dipping the O1 into diluted fluorescein and turn on the system laser at 488nm. A green light sheet should be visible. Pictures of the light sheet from “front” and “side” is shown in Figure 18

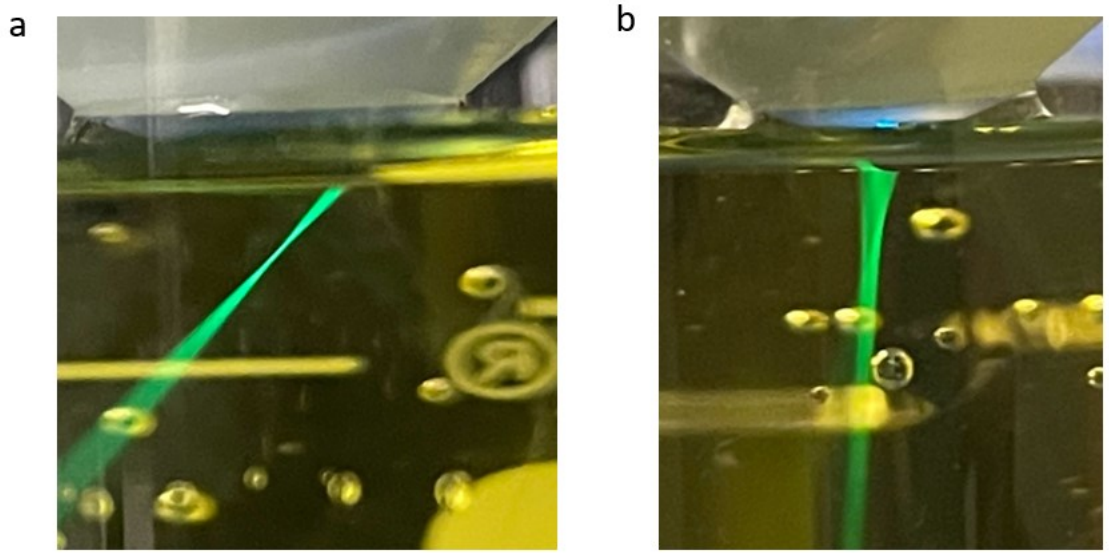

Figure 18 Light sheet output from O1 viewed from a) front; b) sideway

5. Check if the light sheet is output from the center of O1 from the side view. If not, adjust the height of angle system until it is centered
6. Check if the output light sheet is vertical from the front view. If not, adjust the translation stage in X axis using the knob until it is vertical
7. Input a sinusoidal signal to the galvo mirror with amplitude at 0.6V using MATLAB. Details to control galvo mirror using MATLAB can be found in 3.2.3
8. Check if the light sheet is scanning within the diluted fluorescein solution parallelly at front view. If not, loosen the set screw of CL2's cage plate, then move it back and forth gently until the angle of light sheet is kept constant during the scanning
9. Check if the light sheet is focused on the center of galvo mirror. It should be so after step 6-8. If not, it is indication that alignment in module 1 and 2 was not done properly
10. Stop the scanning of galvo mirror and set it back to the reference voltage
11. Adjust the translation stage in X axis until the light sheet is at roughly 45°
    *The light sheet must output from the right edge of the O1 for proper imaging
12. The fine alignment of module 4 is now completed. There is only the angle matching left and it will be done after the tilted alignment between O2 & O3

Table 6 Parts list for module 4

Optical Part	**Part description**	**Part number (Vendor)**
PL	30° Powell lens	LOCP-8.9R30-1.0 (Laserline Optics)
CL1	50mm cylindrical lens	LJ1695RM-A (Thorlabs)
CL2	75mm cylindrical lens	LJ1703RM-A (Thorlabs)
Turning mirror x2	30mm cage turning mirror	CCMG01 (Thorlabs)
Mounting	**Part description**	**Part number (Vendor)**
Rotational cage plate ×3	30mm cage rotational plate	CRM1T (Thorlabs)
Slit	30mm cage compatible slit	VA100CP (Thorlabs)
Manual translation stage	2 axis and rotational stage	XYR1 (Thorlabs)
30-60mm cage adaptor ×2	0.5" thick	LCP33 (Thorlabs)
Lens tube ×2	1" lens tube, SM1 threaded	SM1L10 (Thorlabs)
1.5" post ×3	1/2" optical post	TR1.5 (Thorlabs)
1.5" post holder ×3	1/2" post holder	PH1.5 (Thorlabs)

3.1.5. Tilted Alignment between O2 & O3

The tilted alignment between secondary and tertiary objective is the key of OPM system as it eliminates both spherical aberration and defocusing caused by the tilted imaging plane. As objectives are extremely sensitive to its 3D position, it is vital to provide as much degree of freedom as possible while performing the tilted alignment. A pre-aligned cage system combining O2 and O3 would not necessarily results in a good performance. It is important that all modules are properly assembled prior to this section. A step-by-step procedure for the alignment will be detailed in this section and it is encouraged to modify the procedure based on the actual situation of the system.

After the tilted alignment between O2 & O3, another step needs to be done to precisely match its angle to the light sheet. During this step, fluorescent hydrogel beads (with size range from 50-200μm) could be handy but other simple 3D biological samples such as nuclei-stained cells embedded in collagen gel can also be used. It is important that the structure used in this step is nicely shaped and easy to be imaged. Details to obtain fluorescent hydrogel beads are not included in the procedure.

Tilted alignment between O2 & O3:

1. Remove the last turning cube from O3 and position the filter wheel so the green filter is in use
2. Place a cage compatible iris at the back of the filter wheel
3. Set the galvo to the center position by providing it with reference voltage determined from 3.1.2
4. Position the O3 at around 180° in front of O2 and turn on the alignment laser
5. Position the O3 until a relatively collimated beam is output from its back
   *The laser spot should be a perfect sphere at this point
6. Slightly rotate the O3 counter clockwise with respect to its focal point
   *It is common that the laser spot disappears
7. Slowly move O3 back and forth along the orthogonal line to its optical axis until the laser spot re-appear and passes through the center of the iris
8. Slowly move O3 back and forth along its optical axis until the laser spot is relatively collimated
9. Repeat step 6 to 8 until a tilted angle roughly at 45° is achieved. As the tilt angle increases, the laser spot output from the back of O3 will start to be clipped and forming an olive shape
10. Repeat step 7 and 8 until the output beam is perfectly collimated (confirm by using shear plate) and passes through the center of iris.
    *This step can be extremely tedious and may require many iterations
11. Gently use 2 sets of table clamps to secure the position of module 3
    *Do not use screwdriver. The fine alignment could be altered by over tightening
12. Check if the laser beam is still collimated and passes through the center of iris after securing the position of module 3
13. Gently remove the iris and put back the turning cube and bring in the vertically mounted camera with its tube lens. Making sure the laser spot is hitting the center of camera's tube lens
14. The tilted alignment between O2 and O3 is now finished. The angle matching between the light sheet and O2 & O3 will be detailed in the following section

Angle matching between light sheet and O2 & O3:

1. Prepare 1% agarose solution by adding 0.1g of agarose into 10ml of pure water
2. Microwave the 1% agarose solution for 1 minute with 10s increment. The solution should be transparent after all agarose is dissolved. Be careful not to overheat the solution
3. Wait until the solution cools down and can be handled by hand. Extract $400\mu l$ of the agarose solution into an Eppendorf tube
4. Add in 4 μl of concentrated hydrogel beads into the agarose solution and vortex for 10s
5. Quickly extract 50 μl of the mixture and pipette it into a 35mm petri dish
6. Cover the lid of petri dish and wait until agarose solution fully gelled
7. Add in PBS to fully cover the agarose gel
8. Immerse O1 into the PBS and locate the agarose gel by using bright-field imaging system
9. Adjust the height of sample stage until hydrogel beads are in focus
   *Hydrogel beads should appear to have a very faint boundary within the agarose gel
10. Disable the bright-field system by removing the mirror and turn off the LED. Turn on the system laser and put the camera in live mode with $50ms$ exposure time
11. Adjust the height of sample stage until hydrogel beads are in focus. It may be necessary to move the sample around to locate larger beads.
    *It is common beads are not shown to be spherical at this stage
12. Slowly adjust the translation stage in module 4 in X-axis by using its knob
13. Keep adjusting the translation stage until beads become spherical on camera
    *If multiple beads are captured within the field of view, all of them should be in focus now
14. The angle matching is now finished. The alignment for the entire OPM system is completed

3.1.6. Sample Stage Design

Due to the dipping nature of the primary objective used in customized OPM system, it is deemed that a shallow container with diameter with at least 30mm should be used to house the sample. As a result, a 35mm petri dish is chosen as the primary container and the sample stage is design around it.

Weighing in the cost and ease of use, a combination of Picard USB 4D stage and lab jack (Thorlabs, L490) was chosen. However, the mounting of Picard USB 4D stage was designed to house a thin and long tube used in OpenSPIM[10] system. As a result, a customized stage arm is designed to fit a 35mm petri dish as shown in Figure 19. The bottom of the petri dish mount was designed to be hollow, so that a collimated LED can be used from the bottom as the light source for bright-field imaging system. It is worth noting that a set screw not shown in the figure was also manufactured to secure the petri dish in place.

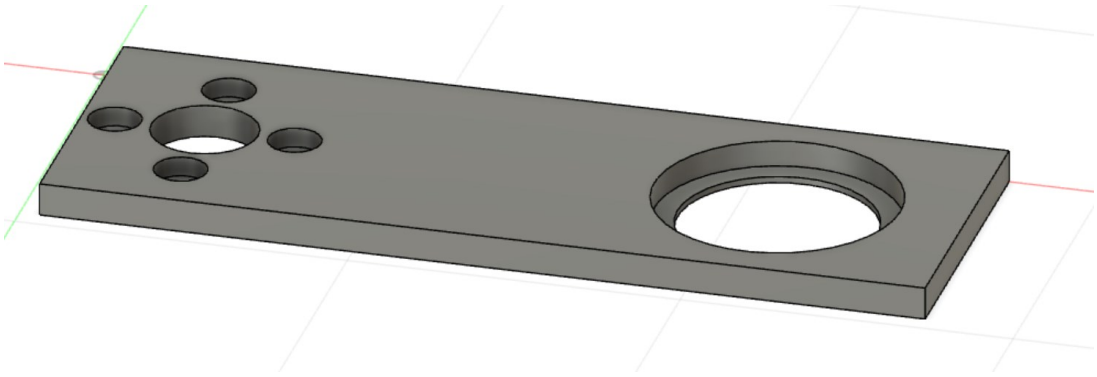

Figure 19 Customized stage arm for Picard USB 4D stage to house 35mm petri dish

The Picard USB 4D stage was mounted on top of the lab jack by using existing threaded holes and the customized sample stage was simply placed under the O1. The finished sample stage is shown in Figure 20. The position of the sample stage was manually adjusted before using a table clamp to secure its location. The rapid movement in z-axis when swapping the sample was accomplished by using the lab jack while fine movement during the imaging was controlled through Picard USB 4D stage. Finally, the Picard USB 4D stage was solely controlled by the software designed by Picard Industries. As a result, the control of sample stage will not be included in the following sections.

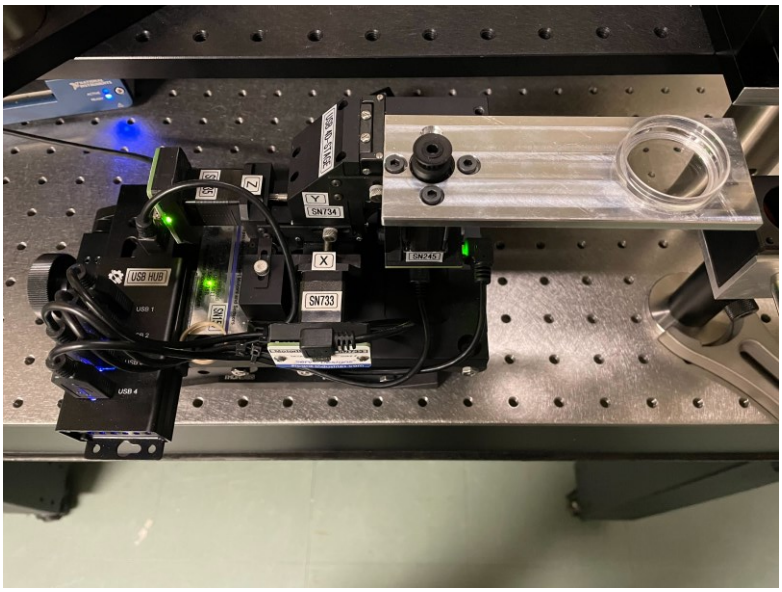

Figure 20 Customized sample stage designed to house one single 35mm petri dish

3.2. System control and automation

3.2.1. High level architecture

As there is no readily available software for integrated control and automation for all components used in the system. A combination of commercial software and home-written MATLAB code was used for the purpose of system control and fast imaging. A high level control architecture is demonstrated in Figure 21. Shown in the right side of the diagram, components such as laser, sample stage and bright-field camera are solely controlled by using accompany commercial software. On the other hand, MicroManager was used to communicate with the sCMOS camera for general purposes such as live viewing. Functions available in MicroManager allows an easy preliminary analysis of the image, making it suitable for common usages. However, the automated image acquisition was made possible by synchronizing between the sCMOS camera and galvo mirror using MATLAB. The versatility of MATLAB together with its capability to generate fast and precise analog signal making it the ideal choice for automated image acquisition. Notes for using commercial software for laser, sample stage and bright-field camera will be included in appendix A.4 and customized control will be detailed in section 3.2.2 to 3.2.4.

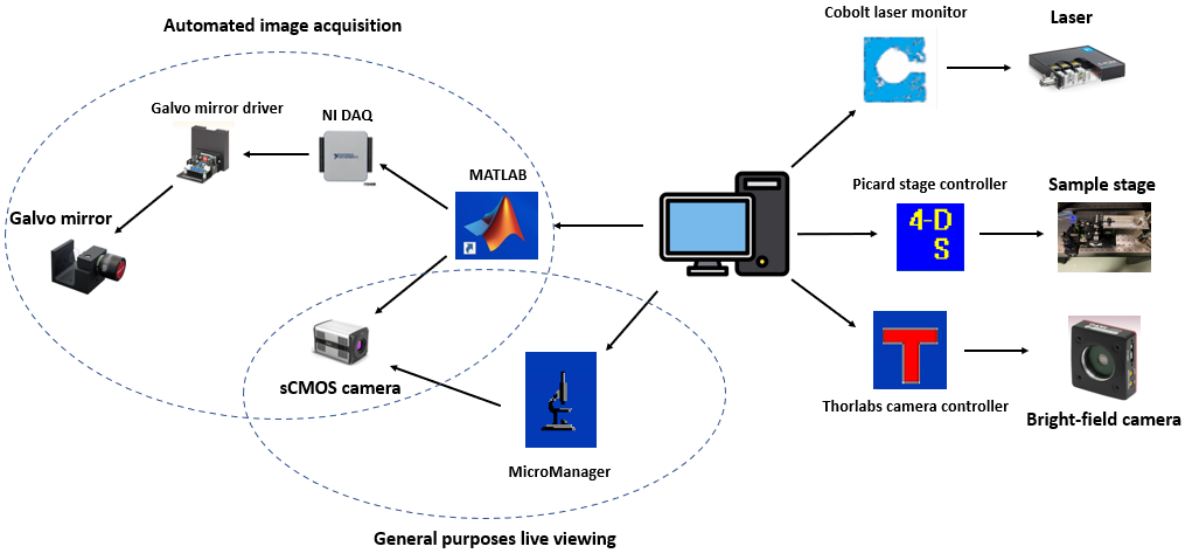

Figure 21 Overall architecture of system control for customized OPM

3.2.2. Andor Camera

Camera is the most control heavy element within the entire system and 2 different pathways were used for different tasks as shown in Figure 21. For live viewing and other general operations, an open-source software named MicroManager was used[37,38]. By using SDK3 purchased from Oxford Instrument, MicroManager can access all functions and parameters of the camera, making general operations easy and smooth.

However, MATLAB was used to control the camera for automated image acquisition. This is because MicroManager do not support analog signal generation required by the galvo mirror control. Detailed MATLAB control for automated image acquisition will be presented in 3.2.4.

3.2.3. Galvo Mirror

As galvo mirror dictates the entire volumetric scanning within the system, fine control is required. It is controlled by the analogue signal where 0.5V corresponding to 1 degree of rotation. Furthermore, the sensitivity can reach a change of 0.0004V. Thus, a NI DAQ board (National Instrument, NI6009) was used to generate fast and precise analogue signals.

The desired voltage or sinusoidal waveform used for 3.1.1 and 3.1.4 was first generated in MATLAB. Afterwards, a connection between MATLAB and DAQ was established before the signal was sent out. For sinusoidal output, the speed of oscillation can be easily adjusted by changing either the frequency or sampling rate. Detailed code is shown in A.1.

3.2.4. Camera-Galvo Mirror Synchronization and automated image acquisition

To achieve fast volumetric imaging, synchronization between the galvo mirror and camera must be done. MATLAB was used to achieve such objective and corresponding SDK3 was purchased from Oxford Instrument to allow accessing of camera properties. Detailed code for synchronization and automated imaging can be found in A.2 which was adapted from the kinematic series sample code provided by Oxford instrument. During the automated imaging session, triggering mode of the camera was set to internal with constant exposure time defined by the user. Afterwards, the memory buffer required for each frame was allocated before the imaging session starts. The image acquisition was controlled by a while loop with the position of galvo mirror first been set followed by a 2ms wait time before the frame was captured. Given the relatively long exposure time range from 50-250ms, forcing a wait time doesn't hinder the speed of volumetric imaging significantly.

3.3. System characterization

After the OPM is assembled, characterization is required to obtain the operating parameters of the system. To access the quality of light sheet, per pixel distance and resolution of scanning step, a positive resolution test target (Thorlabs, R1L1S1P) was used. Afterwards, 200nm fluorescent beads embedded in 1% agarose was used to obtain the point spread function of the system. Procedure of the characterization will be presented in detailed while the results will be shown in section 4.1 to 4.4.

3.3.1. Thickness of the light-sheet and per pixel distance

To characterize the thickness of the light sheet and the per pixel distance, grid with 5 μm wide line and 100 μm pitch distance was used. The resolution test target was first immersed using PBS and the grid was located using bright-field imaging system. Afterwards, laser at 488nm and 18mW was used with the LED light kept on. By using live viewing mode in MicroManager with exposure time set at 25ms, a bright line of laser and blurry grid was observed. The orientation of the resolution test target was then adjusted using tweezer until the light sheet was parallel to the grid line. The LED light was then turned off and only spots where laser line intersects the grid line was visible. The 4 images of the same bright spot were then taken with system magnification set at 9.31X, 13.3X, 17.96X and 26.67X.

3.3.2. Scanning step size characterization

To correlate the voltage applied to galvo mirror and the travelling distance of light sheet resulted from it, concentric circles with 100 μm spacing and 5 μm line width were used. After immersing the resolution test target using PBS, bright-field imaging system was used to locate the concentric circles. Afterwards, 488nm laser at 18mW was used with 50ms exposure in MicroManager. With LED light kept on, Picard USB 4D stage was used to find the location where the laser line is tangent to one of the circles. Both LED and MicroManager were then turned off before switching to automated image acquisition using MATLAB.

By applying a series of voltage change at 0.0008V to galvo mirror, 500 images were taken with 150ms exposure per frame. By analysing the number of steps required for light sheet to travel through 100 μm, a correlation between applied voltage and scanning distance can be established.

3.3.3. Point spread function (PSF)

To obtain the point spread function of the system, TetraSpeck 200nm fluorescent beads were embedded into 1% agarose gel before the imaging. A detailed step by step procedure is shown below.

PSF measurement with nanosphere embedded in 1% agarose gel:

1. Measure roughly 0.1g of ultra pure agarose powder using a glass bottle with plastic cap
2. Add in enough pure water to achieve 1% mass to volume ratio
3. Heating up the mixture using microwave for 1min with 10s interval
4. While waiting for the agarose solution to cool down, prepare 200nm fluorescent beads by ultrasonicating the stock for 3 minutes followed by 10s of vortex
5. After agarose is slightly cooled, extract 200 μl of the solution and adds in 2 μl of fluorescent nanobeads
6. Vortex for 10s
7. Extract 10 μl of the mixture and pipette it onto a petri dish
8. Wait until the droplet gels and then add enough PBS to fully cover it
9. Bring the immersed droplet under microscope and locate it using bright-field imaging system
10. Turn on 488nm laser and set it at 18mW. Set the exposure of camera at 75ms and start the live viewing
11. Using Picard USB 4D stage to locate fluorescent nanobeads, they should appear to be oval-shaped dots on screen, adjust the laser power and brightness level as needed
12. Making sure no pixel is over saturated before taking the image
13. Crop the image to include only 1 single bead from the focal point, the oval shaped bead image is the point spread function of the system

3.4. Midbrain organoids

The mid brain organoids used as imaging samples were provided by colleagues whose research concentrates on understanding of the neural development. To put it in short, the iPSC line was obtained through the Neuro 's C-BIG repository. The cell line was maintained at 37℃ with 5% CO_2 on Matrigel-coated plates in feeder free media (mTeSR, StemCell Technologies) with daily media change. Cells were passaged at 70% confluency with spontaneous differentiation area removed manually.[4] Afterwards, midbrain organoids were generated following Mohamed's protocol[35]. Poly N-isopropylacrylamide (NIPAAM) beads stained with Texas red were embedded during the development process.

Organoids were fixed overnight at 4℃ on day 7 by using 4% paraformaldehyde, washed thrice for 15min using PBS before been permeabilized by using 0.1% Triton-X. Organoids were then stained with phalloidin FITC for filamentous action at 1:25 and Alexa 555 for Tuj1. Organoids were then tissue cleared following CUBIC tissue clearing protocol.[6] Finally, organoids were placed in 96-well plate before been imaged using Opera Phenix.

After images were obtained using Opera Phenix, organoids were removed from tissue clearing solution and washed using PBS. As a result, tissue cleared organoids transformed back into non-cleared state. Afterwards, several organoids were selected and stained with SYTOX for nuclei at 1:10000. Finally, organoids were placed individually at the center of a 35mm petri dish before been encased by 1% agarose.

3.5. NIPAAM beads

The fabrication process of NIPAAM beads utilizes two phase oil emulsion with step by step protocol published by Campbell et. al[39]. In addition, the study of tissue mechanics was not the focus on this project and thus the mechanical properties of NIPAAM beads are not reported.

In short, 6% polyglycerol polyrincinoleate surfactant was prepared in kerosene and 1% ammonium persulfate (APS) was prepared in PBS. The pre-polymerized poly-NIPPAM solution was prepared with 150 μl of 20% NIPAAM, 50 μl of 2% Bis-acrylamide, 697.5 μl of PBS and 1.5 μl of Tetramethylethylenediamine (TEMED). Kerosene solution was deoxygenated by placing a magnetic stir bar into the tube before capping with rubber septum stopper. Two 25G non-coring needle were inserted into the tube with one above the liquid surface and the other immersed to the bottom. Nitrogen gas was passed through the kerosene for 20min. NIPAAM beads were formed by mixing the pre-polymerized solution and APS solution followed by quick vortex. The mixture was then transferred into the kerosene solution using another needle followed by another 5-10 second of vortex. The combined solution was gently mixed using the stir bar and was left for 15min for polymerization. The emulsion was then divided into several tubes for easier washing steps. A total of 3 kerosene washing, and 3 PBS was performed by 3min of centrifuge at $14800 \times G$ followed with aspiration and resuspension using corresponding solution. Finally, NIPAAM beads were allowed to sit in PBS stored in 4℃ fridge overnight to allow swelling.

Before embedding NIPAAM beads into organoids, its surface was functionalized. To do so, beads were first suspended in a 0.05 mg/mL solution of sulfoSANPAH in PBS and sterilized under 36W UV light for 4 minutes. After that, beads were washed using PBS once and incubated in 0.05mg/ml Type I collagen solution overnight in 4℃ fridge. Finally, beads were washed with PBS once more before been stored in fridge.

3.6. Post-Processing

Raw images obtained from the customized OPM system were first cropped and intensity adjusted using Fiji. A blind deconvolution based on maximum likelihood with 15 to 30 iteration was then applied using MATLAB. Either confocal style theoretical PSF or experimental PSF was used as the initial guess. It should be noticed that the tilt alignment used in OPM affects the light transmission spatially due to the non symmetric curvature each ray encounters. As a result, experimental PSF obtained from different locations of the image would not be the same which complicated the deconvolution using traditional model-based algorithms. The experimental PSF should be cherry-picked from the center of the image and only used as an initial guess for blind deconvolution.

For stack of images, a shear correction was also applied so that the tilted image plane can be visualized properly as a conventional z-stack. The shear correction is in unit of pixels and is correlated with the tilt angle of the light sheet. It should be noticed that truncation in pixel counts was needed occasionally during the correction. As a result, the accumulation of error throughout the large stack of images with extremely small scanning step could potentially hinder the quantitative analysis or 3D reconstruction.

4. Results

After the customized OPM system is constructed, it is essential to characterize essential parameters before imaging biological samples. As described in section 3.3, a positive resolution testing target with multiple types of grids from Thorlabs was used for such purpose. The $100\mu m$ grid was used for light sheet and pixel characterization while the concentric circles were used for scanning resolution characterization. By using targets with larger size, it reduces the error associated with image interpolation. Afterwards, 200 nm fluorescent beads embedded in 1% agarose gel were used to obtain the point spread function of the system with laser wavelength at 488nm. Furthermore, images of 2D grids were obtained and demonstrated for both bright-field imaging system and customized OPM. It demonstrated the capability of the system to view a conventional imaging plane and skewing that may associated with it.

With fully characterised OPM system, fixed, non tissue-cleared mid brain organoids were imaged for SYTOX stained nuclei, Phalloidin FITC stained actin, Alexa 555 stained Tuj1 and Texas red stained NIPAAM beads. Resulting images were compared with images obtained using commercial confocal microscope (Opera Phenix) using fixed, tissue-cleared mid brain organoids.

Both nuclei and actin were chosen to be stained due to their ability to reveal the location and cytoskeleton structure of cells within the tissue. Meanwhile, as a marker produced exclusively by neurons, Tuj1 was chosen as it is commonly used for the study of neuron differentiation.

It should be noticed that the exact value NA for customized OPM is non trivial, makes it hardly comparable with other microscopy systems. The tilted alignment between O2 and O3 causes loss of NA and the resulting NA is negatively related to the tilting angle. As described in section 3.1.5, the tilting angle can only be coarsely controlled and can vary each time during the re-alignment. As a rule of thumb, 30-40% of primary objective's NA can be preserved using setup described in this work.

4.1. Per pixel distance

The per pixel distance characterization was done by setting T3 at 70, 100, 135 and 200mm. It corresponding to an overall system magnification at 9.61X, 13.33X, 17.96X and 26.67X. As

described in section 3.3.1, laser at 488nm was used with power set at 18mW and camera exposure time set at 25ms.

After rotating and cropping the image to include only 2 bright spot, number of pixels involved for 105 μm spacing (100 μm pitch plus 2.5 μm of line width on each side) was computed as shown in Figure 22. Results showed that 0.7241, 0.5357, 0.407 and 0.2933 $\mu m/pixel$ was achieved with magnification at 9.61X, 13.33X, 17.96X and 26.67X.

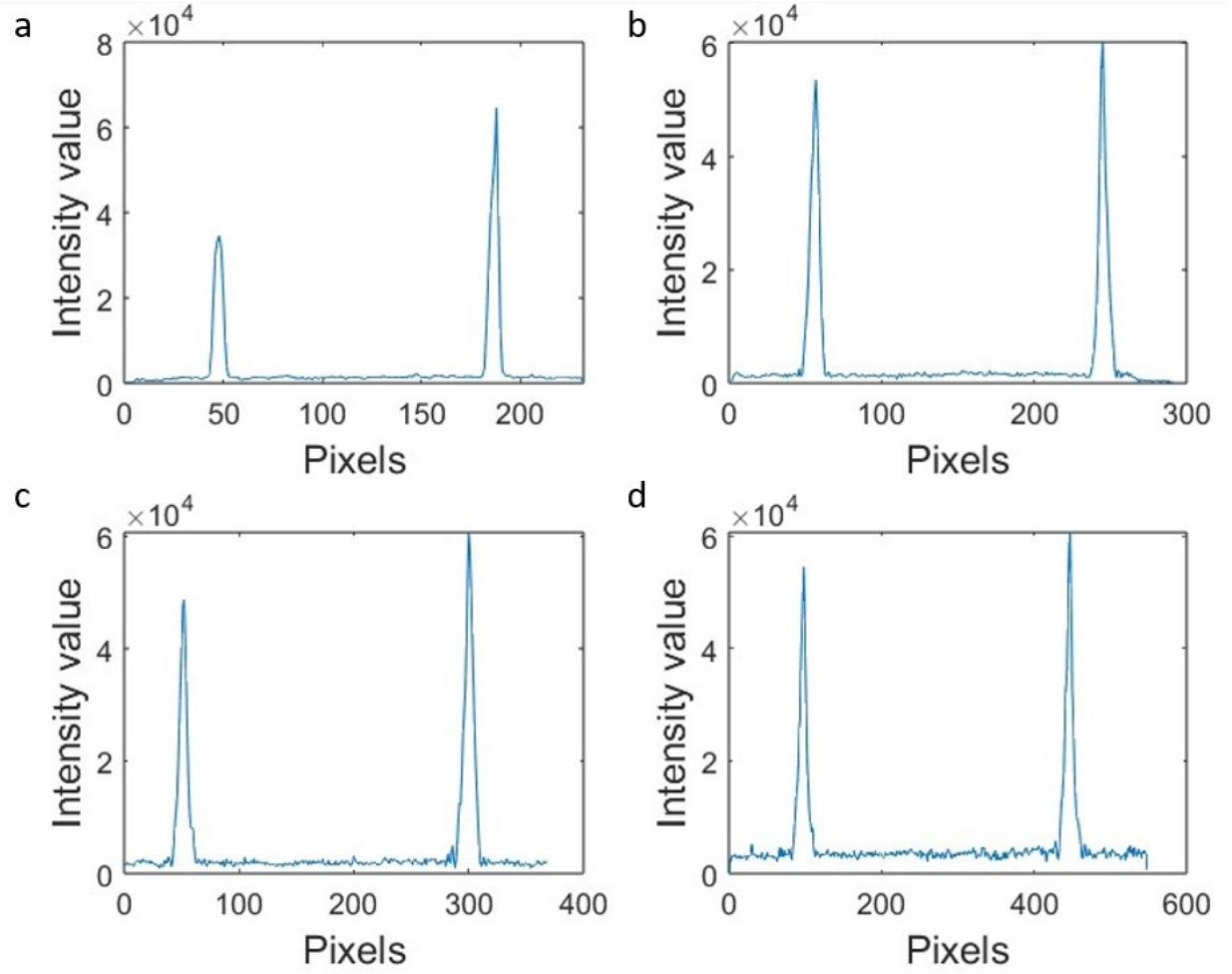

Figure 22 Pixel spacing over 105 μm distance with magnification at 9.61X, 13.33X, 17.96X and 26.67X

4.2. Thickness of light sheet

With per pixel distance calibrated, the thickness of the light sheet can be easily calculated using the full-width-half maximum (FWHM) of spots on grid line been illuminated as shown in Figure

23. As the thickness of light sheet was constant throughout full range of magnification, FWHM for all 4 magnifications were plotted as shown in Figure 24 and values were calculated for comparison. By averaging values obtained from all 4 settings, a light sheet thickness at 3.64 ± 0.1 μm was obtained.

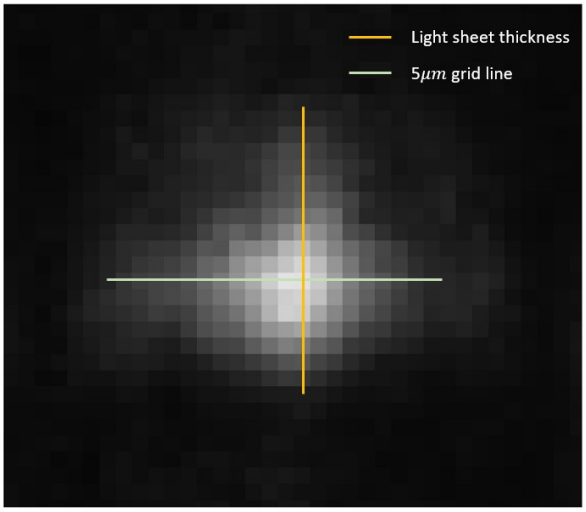

Figure 23 Enlarged spot on grid line where it is illuminated by the light sheet oriented in orthogonal direction. Horizontal line represents the line thickness at 5 μm and FWHM of vertical was used for calculation of light sheet thickness

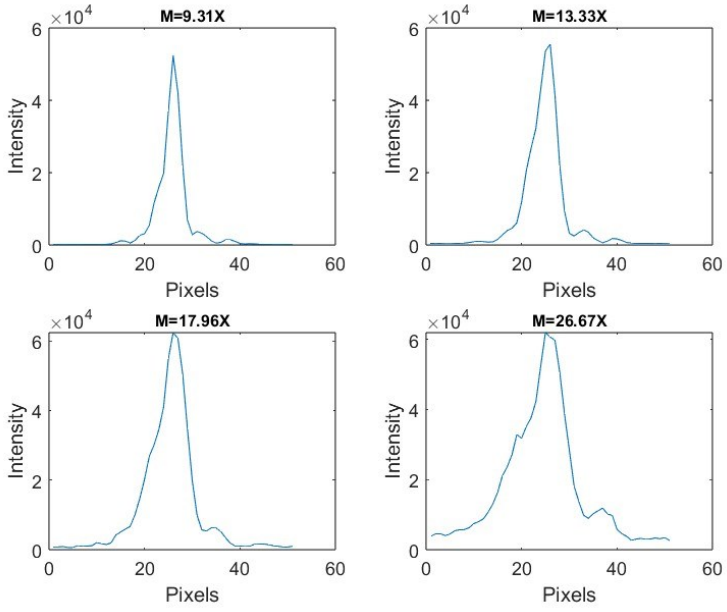

Figure 24 FWHM used for calculation of light sheet thickness with all 4 magnification settings

4.3. Scanning step size characterization

To correlate voltage applied for galvo mirror with linear translation of light sheet on sample, concentric circles with arc line width at $5\mu m$ and spacing at 100 μm were used. As described in section 3.3.2, a 0.0008V increment was applied to galvo mirror and a total of 500 images were collected. The simplified process is demonstrated in Figure 25. Results showed that a total change of 0.3232V was need for a linear translation of 100 μm. Thus, the voltage to translation correlation was found to be $0.003232 V/\mu m$ and the step size resolution was calculated at 0.124 μm.

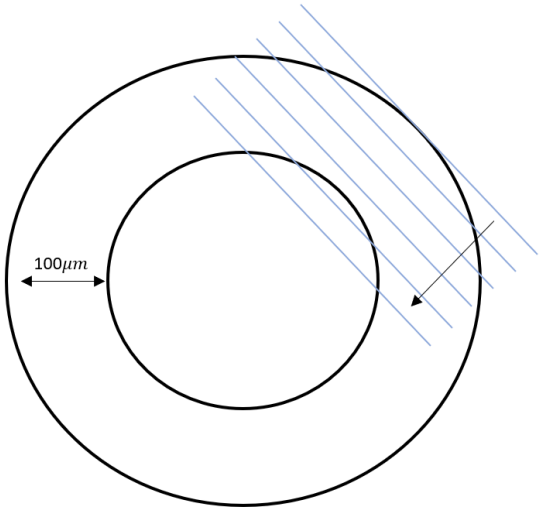

Figure 25 Illustration of the process for scanning step resolution characterization

4.4. Point spread function

To better facilitate post processing such as deconvolution, experimental point spread function was obtained. As described in section 3.3.3, fluorescent nanobeads at 200nm were embedded using 1% agarose. Laser at 488nm with power set at 20mW was used for illumination and an exposure time at 100ms. The magnification of the system was set at 26.67X and the resulting PSF is shown in Figure 26.

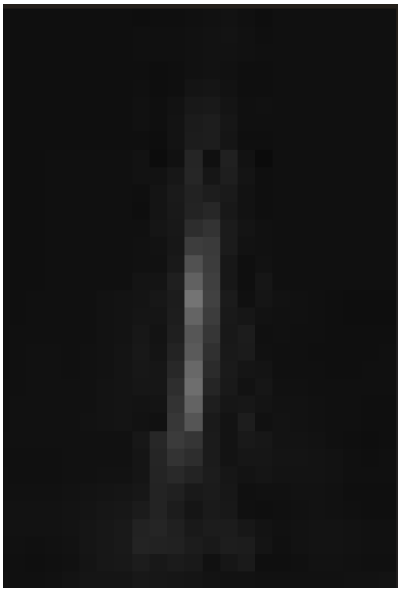

Figure 26 Point spread function of the customized OPM system obtained by using 200nm fluorescent beads (TetraSpeck) embedded in 1% agarose gel and imaged using 488nm laser with power at 20mW

4.5. Bright-field image of calibration grid

To demonstrate the proper alignment of bright-field imaging system, a 50μm calibration grid with 5 μm wide lines was imaged and shown in Figure 27. It should be noticed that this image was taken with a 100mm lens used as T3. As a result, the overall magnification was set at 5.83X which is different from the setup described in section 3.1.1.

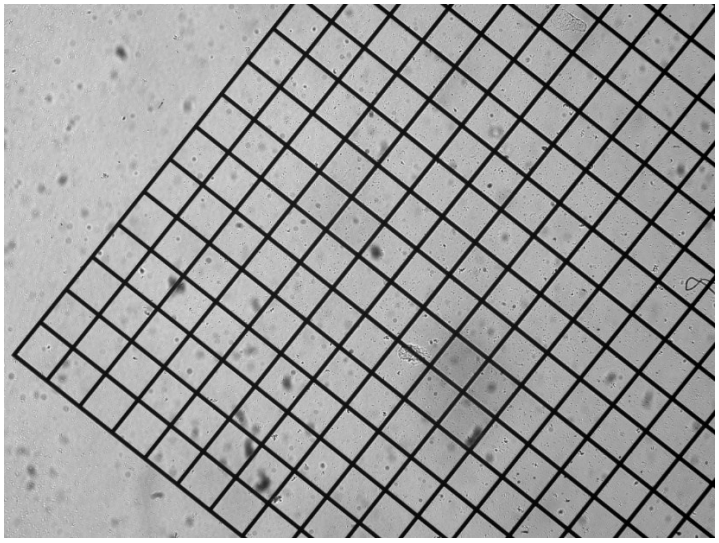

Figure 27 50 μm calibration grid imaged under bright-field imaging system

4.6. Reconstructed 2D calibration grid using customized OPM

Although the customized OPM was designed for 3D structural imaging purposes, it still poses the ability for conventional 2D imaging. Figure 28 shows the same calibration grid used in section 4.5 been imaged under customized OPM with magnification at 13.33X. However, the raw data can be drastically different compared with those obtained using conventional microscopy system. When a tilted light sheet illuminating the entire y-z plane, it intersects with a conventional x-y plane at a line. Thus, a stack of line images is required to reconstruct the entire 2D images lie on a conventional plane. Individual line image needs to be translated according to its position within the stack before applying z-projection. The Fiji script[40] used for stack translation can be found in section A.3. Furthermore, the de-scanning of galvo mirror ensured that the line stays stationary when been projected onto the camera. As a result, an incremental translation of the image stack is required for proper reconstruction. Finally, a de-skewing compressing the diagonal of grid was applied to compensate for the tilted alignment between O2 and O3.

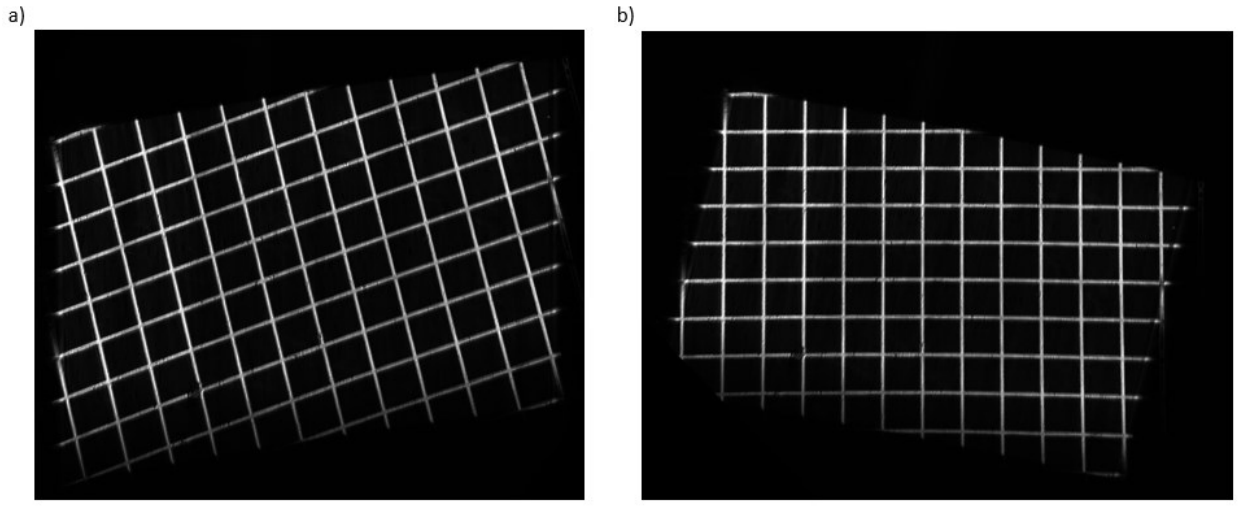

Figure 28 a) 50 μm calibration grid imaged under OPM before applying de-skewing. Intensity adjusted, stack translated and z-projection was applied. b) 50 μm calibration grid imaged under OPM after applying de-skewing

4.7. Comparison of brain organoids images between OPM system and Opera Phenix

To demonstrate the imaging capabilities of the customized OPM system, fixed, non-tissue cleared organoids were imaged for SYTOX stained nuclei, Phalloidin FITC stained actin and Texas red

stained NIPAAM beads. Images for actin, Tuj1 and NIPAAM beads were compared with those obtained from Opera Phenix using the same, but tissue-cleared organoids.

For all images obtained from Opera Phenix, 10X air objective with NA at 0.3 was used. The exposure time for images of NIPAAM beads were set at 200ms while others were set at 180ms. Furthermore, a binning of 2 was applied to all images obtained from Opera Phenix. It should be noticed that the laser power for Opera Phenix can only be controlled as percentage, while OPM system directly adjusted the precise laser power at source output. As a result, no comparison on laser power between two systems can be made.

4.7.1. SYTOX stained nuclei

Nuclei images were demonstrated in green channel by using Sytox green staining with excitation/emission at 504/523nm. A laser at 488nm was used as the excitation and the emission filter with center band at 525nm was used. During the imaging session, a laser power at 3mW was used with camera exposure time set at 50ms. The zoom lens T3 was set at 100mm which gives an overall system magnification of 9.31X. It should be noticed that the Sytox staining was applied after the sample previously stained with Phalloidin FITC already. Though brightness of Sytox is way stronger compared with FITC, the fluorescent light emitted from actin could still be a potential source of extra background noise.

After obtaining the raw image, it was first intensity adjusted and cropped. A confocal style theoretical point spread function generated using Fiji[41] was then used as an initial guess for blind deconvolution. A total of 30 iterations were used and the resulting image is shown in Figure 29. As the image represents a tilted plane at ~45° into the organoid, a gradient of blurry from top to the bottom of the image was expected and observed.

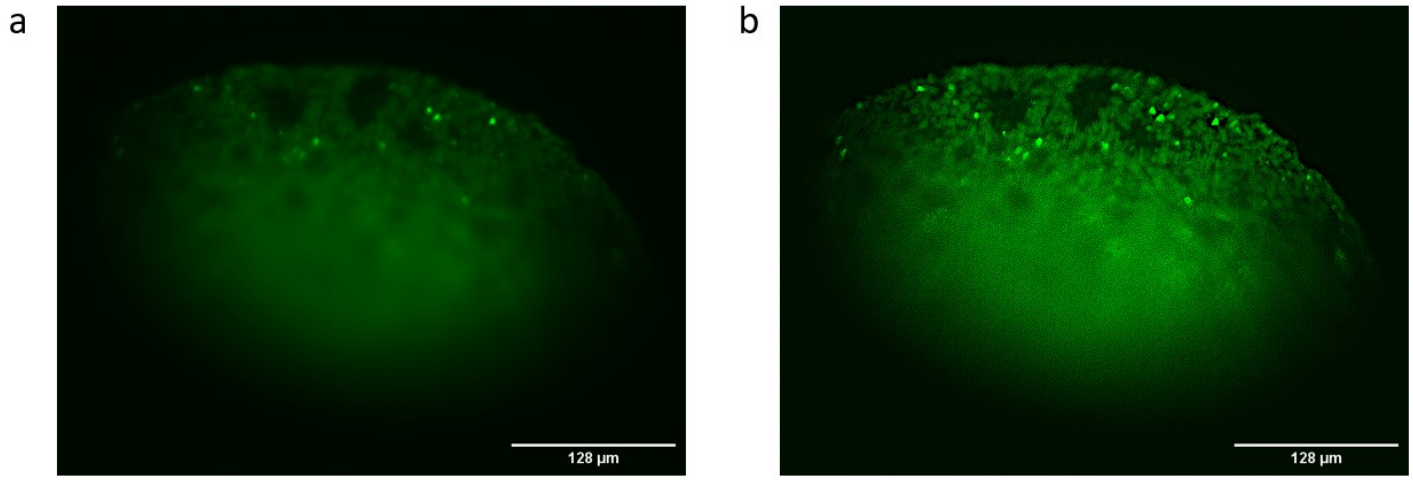

Figure 29 Image of non tissue cleared mid brain organoids with Sytox stained nuclei under 9.31X configuration. A laser power at 3mW with exposure time at 50ms was used during the imaging. a) raw image without deconvolution b) image after adjusting intensity range and 30 iterations of blind deconvolution was applied using theoretical PSF

4.7.2. Phalloidin FITC stained actin

Actin images were demonstrated in green channel by using Phalloidin FITC with excitation/emission at 490/525nm. A laser at 488nm was used as the excitation and the emission filter with center band at 525nm was used. During the imaging session, a laser power at 18mW was used with camera exposure time set at 150ms. The zoom lens T3 was set at 70mm which corresponding to an overall magnification of 9.31X. After cropping and adjusting intensity of the raw image, 20 iterations of blind deconvolution was applied and resulting image is shown in Figure 30.

In comparison, actin image obtained using Opera Phenix with tissue-cleared organoids is shown in Figure 30. The exposure time was set at 180ms with a binning of 2. Raw images were cropped, and intensity adjusted, but no deconvolution was applied.

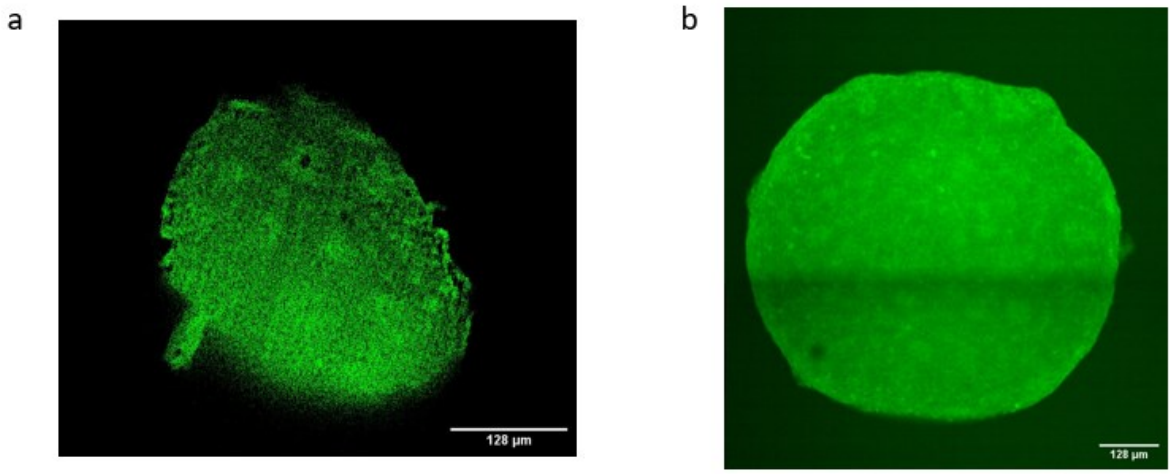

Figure 30 a) Image of non tissue cleared mid brain organoids with Phalloidin FITC stained actin under 9.31X configuration. A laser power at 18mW with exposure time at 150ms was used and no binning was applied. Intensity range of the image was adjusted before applying 20 iterations of blind deconvolution for post processing; b) Image of the same channel using tissue cleared mid brain under Opera Phenix. Exposure time at 180ms was used

4.7.3. Alexa 555 stained Tuj1

Images of Alexa 555 stained Tuj1 with excitation/emission of 555/580nm were collected using laser at 561nm together with an emission filter center at 620nm. During the imaging session, the laser power was set at 8mW with 50ms camera exposure time. The organoid was purposely elevated to bring the bottom section of the organoid in focus. Raw image was cropped, and intensity adjusted before applying 25 iterations of blind deconvolution using experimental PSF. The resulting image is shown in Figure 31a.

In comparison, images obtained using Opera Phenix with tissue-cleared organoids were demonstrated in Figure 31b. The exposure time was set at 60ms with a binning of 2. Raw images were cropped, intensity adjusted, and no deconvolution was applied. It should be noticed that three NIPAAM beads were also visible within the picture due to overlap of excitation and emission band between Alexa 555 and Texas red.

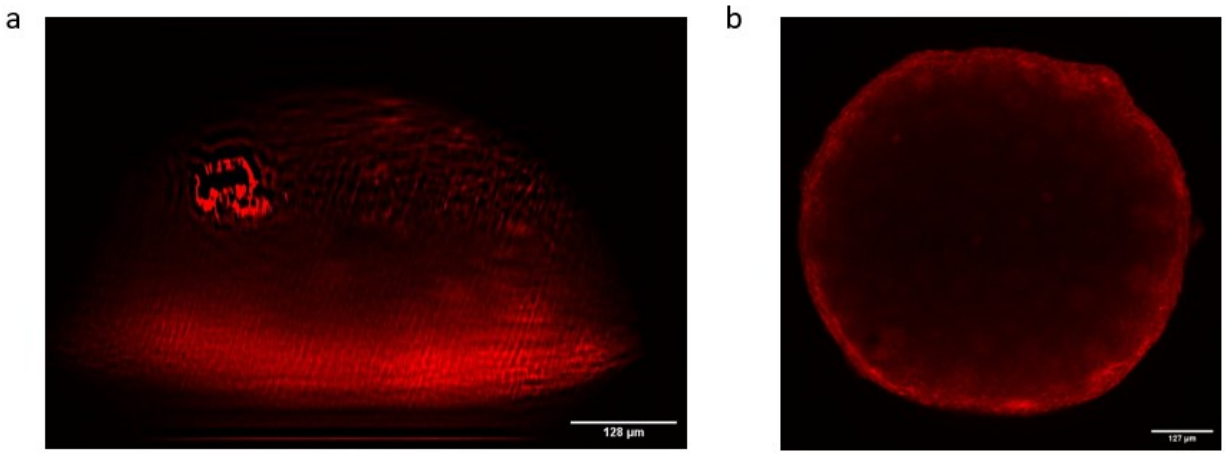

Figure 31 Image of non tissue cleared mid brain organoids with Alexa 555 stained Tuj1 under 9.31X configuration. A laser power at 5mW with exposure time at 50ms was used and no binning was applied. Intensity range of the image was adjusted before applying 25 iterations of blind deconvolution for post processing

4.7.4. Texas red stained NIPAAM beads

Image of Texas red stained NIPAAM beads with excitation/emission of 567/615nm were collected using laser at 561nm together with an emission filter center at 620nm. During the imaging session, the laser power was set at 5mW with 50ms camera exposure time. As the excitation and emission band of Alexa 555 overlapped with that of Texas red NIPAAM beads, features from both staining showed up within raw images. Given the intensity of NIPAAM beads were significantly higher than that of Tuj1, contrast of raw images was adjusted so that only beads remained. The resulting image is shown in Figure 32a with dotted red circle representing the boundary of organoid.

In comparison, images collected using Opera Phenix with tissue-clear organoids were also demonstrated in Figure 32. Similarly, channel overlapping resulted in a mix of features from both Tuj1 and NIPAAM beads. As the brightness of NIPAAM beads were too low to be highlighted by adjusting contrast, raw images were only cropped, and intensity adjusted. Yellow circles were used to highlight the location of NIPAAM beads within the organoid.

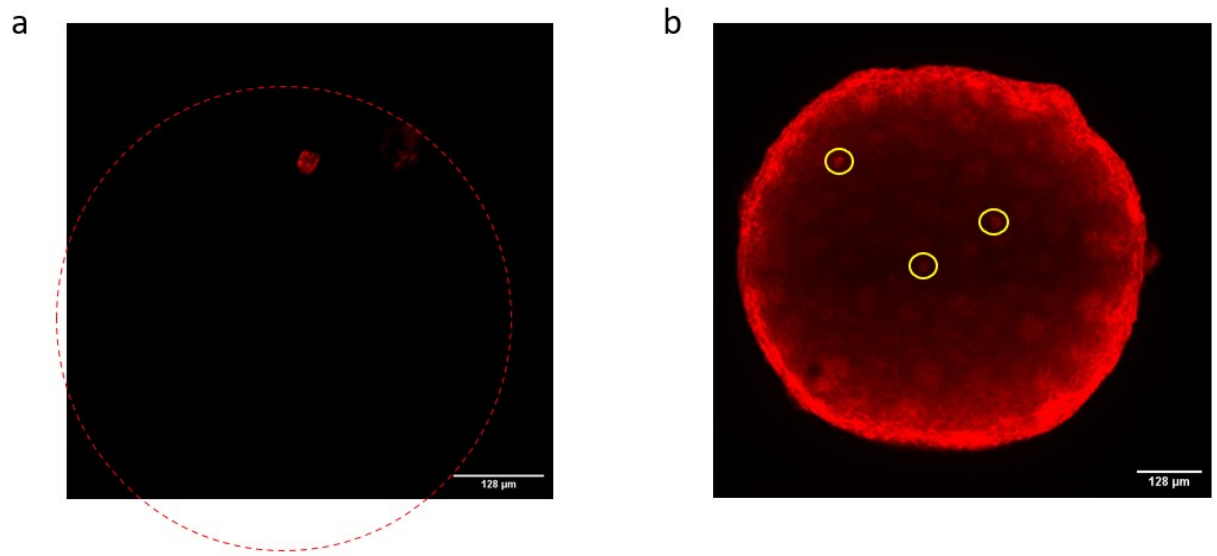

Figure 32 a) Image of non tissue cleared mid brain organoids with Texas red stained NIPAAM beads under 9.31X configuration. A laser power at 5mW with exposure time at 50ms was used and no binning was applied. Raw images were cropped, and intensity adjusted; b) Image of the same channel using tissue cleared mid brain under Opera Phenix with 200ms exposure. Due to low contrast between beads and background noise, yellow circles were used to highlight the location of beads.

4.8. Effect of blind deconvolution

To examine the effectiveness of experimental PSF as the initial guess used for blind deconvolution, images deconvoluted starting with a confocal style theoretical PSF[41] and experimental PSF were compared. An additional set of Sytox stained nuclei images shown in first row at Figure 33 were used to demonstrate the effectiveness of deconvolution at different imaging depth. Comparing nuclei images with different depth, it was found that the experimental PSF significantly degrade the quality of image at low depth while theoretical PSF performed well. In contrast, more details were revealed when the image at higher depth was treated with experimental PSF. This is also observed in images of Alexa 555 stained Tuj1 where the OPM was focused on the very bottom of the midbrain organoid. In terms of images of Phalloidin FITC stained actin, neither PSF showed significant effect compared to raw images. It is suspect that raw images of actin had relatively low quality compared with other features which hindered the effectiveness of deconvolution.

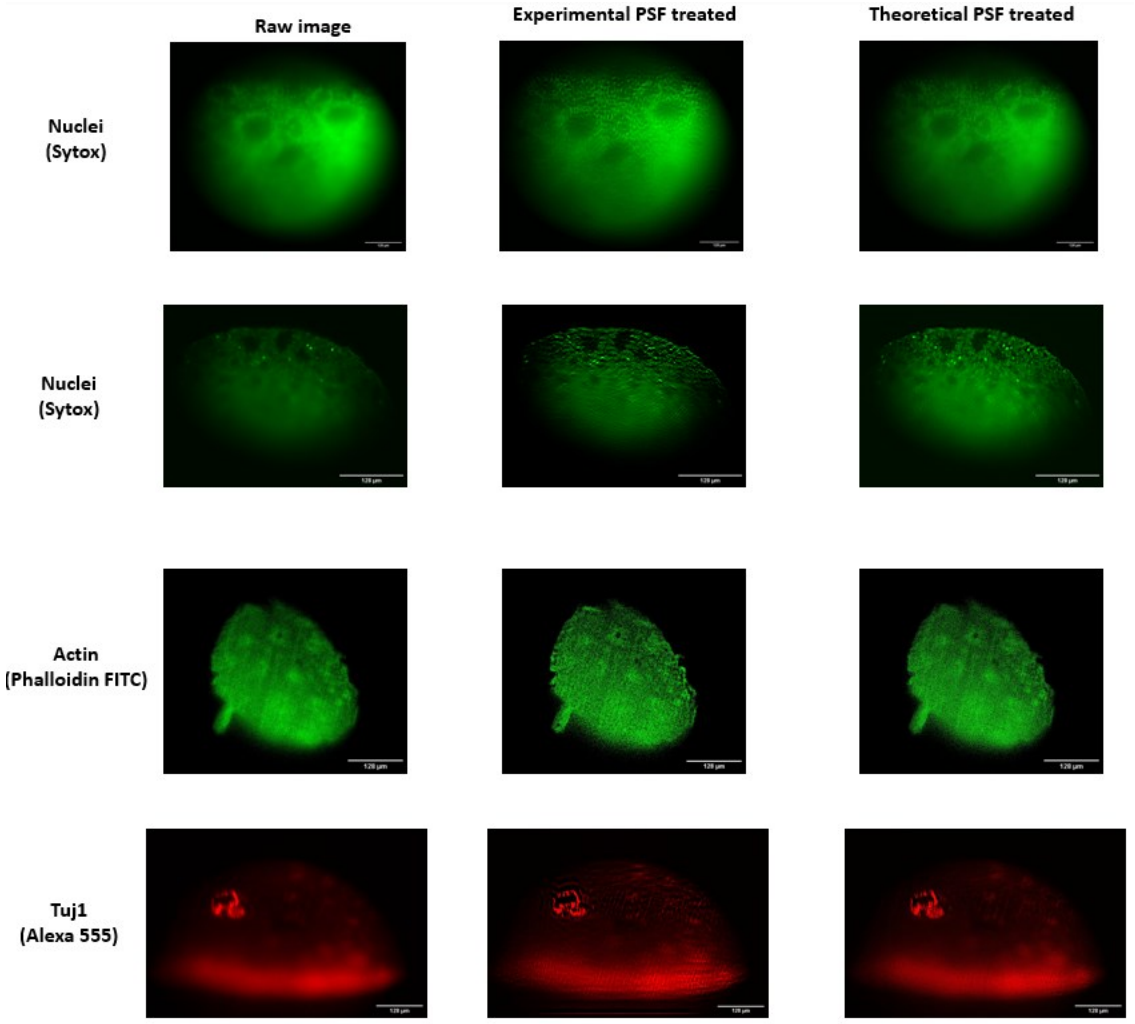

Figure 33 Effect of imaging depth and different PSF used as the initial guess for blind deconvolution.

5. Discussion

Designing a microscope capable of imaging deep into large tissue samples is complicated and often requires trade off between different aspects. In terms of the fluorescent light pathway, the angled alignment between O2 and O3 significantly sacrifice the overall NA of the system, a water dipping objective was selected as O1 to maximize the primary NA while keeping the sample mounting relatively easy. At the same time, air objectives were chosen as O2 and O3 to simplify the alignment procedure and avoids the need of a custom-built water or oil immersion chamber[42]. An objective at 20X was deemed most suitable for the system as it provides an overall magnification ranging from 9.31X-26.67X which matches the need of organoids imaging. Furthermore, the vertical mounting of camera and T3 by using a tripod mount was also deemed mechanically beneficial for the delicate alignment between O2 and O3. Such mounting options separates those extremely heavy components from light optics. As a result, bending due to torque during the alignment would no longer be a concern.

In terms of the excitation pathway, the extremely tight space between S2 and galvo mirror due to 4f alignment. Considering the need to facilitate 3 wavelengths ranging from ultraviolet to red, it leads to the choose of manual swapping dichroic mirrors between wavelengths. To minimize the variability of alignment during the dichroic swapping, an invert-mounted rectangular cage cube was specifically chosen so that the dichroic mirror can be easily changed and auto-alignment at a prefect angle of 45°. In addition, the use of 2 axis manual stage was proved vital for relay of light sheet which further ensures a parallel scanning during the imaging session. On top of relaying, the capability to match the light sheet with the angle between O2&O3 significantly enhances the imaging condition. Furthermore, adjusting the angle of light sheet became the only way for fine alignment, as there lacks method to indicate precise angle between O2 and O3. Finally, optics with 2'' diameter were chosen for both S1 and T1 so that clipping of the light sheet during the scanning can be avoided.

Aside from the design of OPM, the addition of bright-field imaging system is important for the overall operation of the system. Compared with the powerful OPM system, bright field makes the process of locating a sample much simpler. Such capability to bring the traditional x-y plane in focus also proved to be useful for characterization purposes. As the characterization must be done at the focal point of O1 where the light sheet is the thinnest, a 4f aligned bright-field imaging

system could easily bring the sample to the desired height allowing a proper measurement of system's parameters.

In terms of the characterization, results of per pixel distance, light sheet thickness and scanning step resolution revealed the high performance of the customized OPM system. The use of relatively large grid minimized the error caused by the image analysis. The consistency between light sheet thickness calculated under different magnification setting further proved the accuracy of the per pixel distance results. In terms of the characterization of the scanning step resolution, the assumption of perfect parallel translation of light sheet was made. Such assumption is valid given a module 1 with proper 4f alignment and small scanning range is used. Currently, there is no experimental method can be used for verification. Here I purpose that it is possible to scan a large distance over a small grid line and calculate the step required to pass each grid. A linear relation would be the indication of parallel translation.

After raw images were obtained, post-processing mainly focused on the deconvolution using varies PSF. It was observed that deconvolution started with experimental PSF significantly degraded images with relatively small depth, while theoretical PSF successfully enhanced the image quality. On the other hand, experimental PSF showed better performance when treating images with higher depth. Such behaviour is likely caused by the spatially varied experimental PSF originated from different light transmission in OPM. With an experimental PSF cherry-picked from the center of agarose gel, it could hardly be representative to images obtained at shallow region of the organoid. Furthermore, the effectiveness of deconvolution was also limited by the quality of raw images where neither theoretical nor experimental PSF showed much effect on Phalloidin FITC stained actin. In addition, the naturally occurred spatially varied PSF severely limited the choice for deconvolution. As conventional model-based algorithms assume a symmetrical, spatially homogenous PSF. It is proposed that raw images could be subdivided and representative experimentally determined PSF could be applied for each region to achieve better deconvolution results. However, the optimal subdivision as well as matching between regions and PSF are yet to be determined.

In terms of potential 3D reconstruction, shear correction was determined to be vital due to the nature of tilted image plane. Existing software for image analysis or visualization all assume an image plane parallel to the 3D axis. As a result, a consistent image shift would be observed between

each slice when viewing a large stack of sheared images. As mentioned in section 3.6 that, the amount of shift can be computed and compensated by measuring the tilting angle of the light sheet. Finally, to avoid the accumulation of error due to pixel truncation, it would be beneficial to only provide user a set of predetermined scanning step size, which truncation would naturally not be required.

As the customized OPM system was designed for imaging of large 3D tissue samples, the penetration depth is then naturally become a key parameter of interest. However, it is not possible to provide a theoretical value and the experimental value obtained varies significantly between samples. The mismatch of refractive index between immersion medium and tissue samples can cause significant spherical aberration during the imaging and thus reduce the penetration depth. At the same time, the density of biomolecules presented within the tissue sample would also play a significant role. When dealing with tissue with high density of biomolecules like brain organoids, both the emission and excitation pathway suffers from severe scattering and thus reduce the penetration depth. Both problems mentioned could be largely resolved by using tissue clearing solution. However, not only the preparation time of tissue clearing is too long for quality control purpose, the nature of remote refocusing also prevents the proper imaging of tissue cleared samples. The potential upgrade that would allow imaging of tissue cleared samples will be discussed in section 6.

When compared with images obtained using Opera Phenix with tissue-cleared organoids, images from customized OPM system with non tissue-cleared organoids appeared to be comparable or even better, with much shorter exposure time and no binning. Image of Sytox stained nuclei shown in Figure 33 proved that a depth of more than $200\mu m$ can be achieved with non tissue cleared organoids. At the same time, rosettes could be clearly observed within the image as a structural marker. As for the image of Phalloidin FITC stained actin, both Opera Phenix and customized OPM system could not capture fine details of the feature. However, it was shown that OPM system could map out structure of rosettes at the top part of the organoid. It was previously found that rings of actin patterns can be used to determine the location of rosettes[4], and such correlation could enable the localization of rosettes at even deeper depth using images obtained from the OPM system.

Looking at Alexa 555 stained Tuj1, images obtained using Opera Phenix showed significantly higher signal at the boundary of the organoid compared to the center. As a result, it provides little to no information regarding the internal structure. On the other hand, a rosette was brightly labelled and observed under the OPM system. As the penetration depth exceeded expectations during the imaging session, the organoid was purposely elevated to bring the very bottom section into focus. Thus, the image demonstrated that features at the deepest part of a non cleared organoid can also be captured using the customized OPM system given proper choice of marker and associated staining.

Finally, image of Texas red NIPAAM beads obtained using Opera Phenix and OPM system was compared, as the capability to trace hydrogel beads is becoming ever more important in studies of mechanobiology. It should be noted that the staining choice of Texas red was not optimal as it overlaps with the excitation and emission band of Alexa 555. Thus, a mix of features were captured and further complicated the analysis. Theoretically, the brightness of Texas red stained hydrogel beads should far exceed Tuj1 stained with Alexa 555. However, it was shown on the image obtained using Opera Phenix that the brightness of beads is around the same or even lower compared with unwanted Tuj1 signals. It is likely caused by the loss of signal when imaging at the center of organoids, which was observed previously as well. As a result, it was near impossible to clearly isolate hydrogel beads from unwanted features. On the other hand, a distinctive difference between signals from hydrogel beads and Tuj1 can be observed under the OPM system. Therefore, the shape and location of the hydrogel beads can be separated from the remaining features by adjusting the contrast of raw images. Both images of Tuj1 and NIPAAM beads demonstrated the capability of the customized OPM system to obtain strong signals deep inside the non cleared brain organoids. Thus, the OPM system is deemed to be suitable for rapid quality control of brain organoids during their early developmental stages.

6. Direction of Future Work

The customized OPM system presented in the thesis demonstrated its capabilities to image deep into non tissue-clear brain organoids at high speed with low laser power required. By eliminate the need for time consuming tissue clearing protocol, customized OPM deemed to be suitable for rapid quality control of brain organoids during their early development stages. However, if more varieties of tissue samples to be imaged, the significant loss of NA due to the tilted alignment between O2 and O3 could become the bottleneck. The preservation of NA is dictated by the angle of light sheet as well as the NA of O3. Based on the results from modelling[43], high NA water dipping objective (O1) has an optimum tilt angle at around 43°. Thus, there is little room for improvement on the selection of tilting angle. Given the low NA nature of air objective, water dipping objective with custom build immersion chamber has been used as O3[42], but suffers from the much-complicated alignment protocol. Recently, "glass-immersed" objective designed by Millett-Sikking et al.[44] showed its capabilities to achieve $> 95\%$ NA preservation when coupled with a conventional O2 using air objective. As a result, substituting current O3 using the glass-immersed objective is considered as the most simple and immediate improvement for system performance.

Other than the loss of NA, remote refocusing system also imposes constraints on the type of samples to be imaged. As described in section 2.4.1, the magnification between O1 and O2 must equal to the refractive index of the immersion medium. Any deviation from such condition would results in significant amount of spherical aberration. Given the optics with fixed focal distance were used, it prohibits wider application such as tissue-cleared organoids immersed in clearing reagent (refractive index ranging from $1.45 \sim 1.49$) [45,46] or tissues within microfluidic devices. While it is possible to introduce a zoom lens to fast adjust the magnification between O1 and O2, the required range of focal distance is much smaller (88.3-100mm EFL that corresponding to refractive index from 151-1.33) than those offered in commercial zoom lens. Furthermore, the strict 4f alignment also requires such zoom lens to have a static front and back focal plane. Therefore, there is no existing commercial zoom lens that simultaneously satisfy all requirements for OPM system. Inspired by the any immersion remote refocus microscope[47], a zoom lens with dynamic focal distance and static focal plane can be custom built with careful design and alignment. At the same time, it is well-know that most of proteins shows properties as liquid crystal, which

the optical properties changes based on molecular orientation[48]. As a result, the use of such zoom lens not only enables wider application regarding fixed samples for OPM system, but also enhances its capabilities to visualize the dynamics of tissues with temporal change in optical characteristics.

As previously described in section 2.4, HILO microscope utilized a highly inclined light sheet without optical correction for spherical aberration, which limits its field-of-view to the very center of the focal point. Given the magnitude of spherical aberration is a gradient that increases further away from the focal point, it is possible not to create a perfect imaging space for applications only require small field-of-view. One of the typical examples is the super resolution microscopy where only one or few cells are of interest at a time. Traditionally, super resolution method such as single molecule localization microscopy are only performed within 2D samples to achieve the best signal to noise ratio. However, with more interest regarding subcellular behaviours within 3D tissues, single objective light sheet microscope incorporated with adaptive optics (AO) for PSF engineering has been introduced[49,50]. By partially compensating tissue and tilting generated PSF degradation, spherical aberration and defocusing using model-based sensor-less AO algorithm, ideal PSF can be restored at depth up to $90\mu m$ within the tissue. On the other hand, the need for dynamic compensation of multiple types of aberration have put model-based wavefront sensor oriented[51] and image oriented[50,52] sensor-less AO algorithms on strain. Providing the huge dataset resulted from model tuning and complex nature of distortion, machine learning oriented AO algorithms have also gained significant interest[53]. Considering the non optimized deconvolution process due to spatially variant PSF in OPM, AO facilitated PSF engineering could potentially be the solution for better deconvolution results.

To provide a more user-friendly operating environment, the control architecture of the system can also be further improved. As a versatile and powerful open source controlling platform, MicroManager has been used extensively in customized microscopes. However, the fact that it cannot generate analog signal severely limited its use in cutting-edge microscopes. Although plugins have been developed to automate analog dependant electronics[54], they are dedicated to specific usage and not customizable for wider applications. For microscopes based on the principle of OPM, it is common for the scientist to hire external software engineer to develop a dedicated control environment[55,56] or building a control strategy from scratch[13,40]. Thus, it prohibits wider

usage and adaption of their microscope designs. To create a simple-to-use and customizable controlling environment, combination between MicroManager and Python could be viable. Python is known for its versatility and is well compatible with MicroManager[57]. At the same time, the fast-growing open source 3D image processing package[58] further makes it more attractive. Therefore, the generation of analog signal in MicroManager has became the only bottleneck to be overcame. It is proposing that an open source MicroManager plugin dedicated for the generation of analog signal could benefit both the control environment of the customized OPM, and wider applications require analog dependant electronics.

Finally, it was noticed during calibration and characterization process that current method all relies on either 2D standardized target or 3D biological samples. The lack of standardized 3D fluorescent resolution and distortion target makes the development of OPM, or similar system heavily relies on experience. Current 3D fluorescent standards mostly utilize nano or microspheres[59,60] which lacks structural information that can be used for wider characterization purposes. Considering both the need for fluorescent 3D architecture and low cost, the fabrication of 3D fluorescent hydrogel grid using 2-photon lithography is purposed. Hydrogel was selected due to its low cost, versatility and compatibility with commonly used microscopes. By altering the cross linking, the refractive index of the hydrogel can be easily adjusted, making it suitable for objective with all immersion medium. Furthermore, either fluorophore or fluorescent nanoparticles can be easily conjugated with the hydrogel making it suitable for different excitation/emission channels. The use of 2-photon lithography machine is purposed due to the wide range of achievable resolution and high throughput. Protocols to fabricate 3D hydrogel structure as tissue engineering platforms have been well-established[61–63] and resolution ranging from hundreds of micrometers to tens of nanometers could be achieved. Lastly, the isolation and recovery of polymerized fluorescent hydrogel grid could also be accomplished using simple method such as filtration. Thus, it is purposed that fluorescent hydrogel grid fabricated using 2-photon lithography could be a low cost, standardized target for 3D resolution and distortion characterization.

7. Conclusion

In this work, a customized light sheet microscope was built based on the principle of OPM. As well as the control, automation strategy and post-processing pipeline to operate the system. A bright-field imaging system was also incorporated to facilitate sample location prior to the fluorescent imaging session. The microscope was first assembled, calibrated and characterized. Then images of non tissue-cleared midbrain organoids obtained from the customized OPM were compared with those obtained using commercial confocal microscope (Opera Phenix) using tissue-cleared organoids.

The characterization results showed that per pixel distance at 0.7241, 0.5357, 0.407 and 0.2933 $\mu m/pixel$ were achieved under magnification at 9.61X, 13.33X, 17.96X and 26.67X respectively. Furthermore, the thickness of the light sheet was found at 3.64 ± 0.1 μm with scanning step resolution at 0.124 μm. Such results confirmed that high quality optical sectioning can be achieved using this customized OPM system. The automation of high-speed volumetric imaging was achieved by synchronizing between camera and galvo mirror using MATLAB. It was shown that the volumetric acquisition rate over 9 frame per second can be reached with an exposure time set at 100ms.

To verify the capability for structural imaging of non tissue-cleared midbrain organoids for rapid quality control purposes. Images of Sytox stained nuclei, Phalloidin FITC stained actin, Alexa 555 stained Tuj1 and Texas red stained hydrogel beads were obtained. Results showed that a depth of more than 200 μm can be achieved given proper choice of marker and dye. Images of both actin and Tuj1 showed the ability to identify important structural marker in non tissue-cleared midbrain organoids using the customized OPM system was comparable, or even superior to the Opera Phenix using tissue-clear organoids. Furthermore, images of hydrogel beads showed that more signal can be captured from the center of organoids using customized OPM system. Finally, all images obtained from the customized OPM required much shorter exposure time with low illumination power, making it more sample friendly.

Overall, this thesis provided a complete and detailed recipe to assemble, characterize, control and automate a customized OPM system. The system showed strong performance when imaging non

tissue cleared organoids, making it an ideal tool for rapid quality control of brain organoids during early development stages.

8. Reference

1. Qian, X., Song, H. & Ming, G.-L. Brain organoids: advances, applications and challenges. (2019) doi:10.1242/dev.166074.

2. Lancaster, M. A. *et al.* Cerebral organoids model human brain development and microcephaly. *Nature 2013 501:7467* **501**, 373–379 (2013).

3. Lancaster, M. A. & Knoblich, J. A. Generation of cerebral organoids from human pluripotent stem cells. *Nature Protocols 2014 9:10* **9**, 2329–2340 (2014).

4. Cassel De Camps, C. *et al.* Hydrogel Mechanics Influence the Growth and Development of Embedded Brain Organoids. *ACS Appl Bio Mater* **5**, 214–224 (2022).

5. Bershteyn, M. *et al.* Human iPSC-Derived Cerebral Organoids Model Cellular Features of Lissencephaly and Reveal Prolonged Mitosis of Outer Radial Glia. *Cell Stem Cell* **20**, 435-449.e4 (2017).

6. Matsumoto, K. *et al.* Advanced CUBIC tissue clearing for whole-organ cell profiling. *Nature Protocols 2019 14:12* **14**, 3506–3537 (2019).

7. Tomer, R., Ye, L., Hsueh, B. & Deisseroth, K. Advanced CLARITY for rapid and high-resolution imaging of intact tissues. *Nature Protocols 2014 9:7* **9**, 1682–1697 (2014).

8. Hillman, E. M. C., Voleti, V., Li, W. & Yu, H. Light-Sheet Microscopy in Neuroscience. *Annu Rev Neurosci* **42**, 295–313 (2019).

9. Combs, C. A. & Shroff, H. Fluorescence Microscopy: A Concise Guide to Current Imaging Methods. *Curr Protoc Neurosci* **79**, 2.1.1-2.1.25 (2017).

10. Pitrone, P. G. *et al.* OpenSPIM: an open-access light-sheet microscopy platform. *Nature Methods 2013 10:7* **10**, 598–599 (2013).

11. Dunsby, C. Optically sectioned imaging by oblique plane microscopy. *Optics Express, Vol. 16, Issue 25, pp. 20306-20316* **16**, 20306–20316 (2008).

12. Botcherby, E. J., Juškaitis, R., Booth, M. J. & Wilson, T. An optical technique for remote focusing in microscopy. *Opt Commun* **281**, 880–887 (2008).

13. Voleti, V. *et al.* Real-time volumetric microscopy of in vivo dynamics and large-scale samples with SCAPE 2.0. *Nature Methods 2019 16:10* **16**, 1054–1062 (2019).

14. Sanderson, M. J., Smith, I., Parker, I. & Bootman, M. D. Fluorescence Microscopy. *Cold Spring Harb Protoc* **2014**, pdb.top071795 (2014).

15. Lichtman, J. W. & Conchello, J. A. Fluorescence microscopy. *Nature Methods 2005 2:12* **2**, 910–919 (2005).

16. Gustafsson, M. G. L. Surpassing the lateral resolution limit by a factor of two using structured illumination microscopy. *J Microsc* **198**, 82–87 (2000).

17. Fölling, J. *et al.* Fluorescence nanoscopy by ground-state depletion and single-molecule return. *Nature Methods 2008 5:11* **5**, 943–945 (2008).

18. Hell, S. W. & Wichmann, J. Breaking the diffraction resolution limit by stimulated emission: stimulated-emission-depletion fluorescence microscopy. *Opt. Lett.* **19**, 780–782 (1994).

19. Lelek, M. *et al.* Single-molecule localization microscopy. *Nature Reviews Methods Primers 2021 1:1* **1**, 1–27 (2021).

20. Denk, W., Strickler, J. H. & Webb, W. W. Two-Photon Laser Scanning Fluorescence Microscopy. *Science (1979)* **248**, 73–76 (1990).

21. Diaspro, A. *et al.* Multi-photon excitation microscopy. *Biomed Eng Online* **5**, (2006).

22. Ahrens, M. B., Orger, M. B., Robson, D. N., Li, J. M. & Keller, P. J. Whole-brain functional imaging at cellular resolution using light-sheet microscopy. *Nature Methods 2013 10:5* **10**, 413–420 (2013).

23. Voigt, F. F. *et al.* The mesoSPIM initiative: open-source light-sheet microscopes for imaging cleared tissue. *Nature Methods 2019 16:11* **16**, 1105–1108 (2019).

24. Botcherby, E. J., Booth, M. J., Juskaitis, R. & Wilson, T. Aberration-free optical refocusing in high numerical aperture microscopy. *Optics Letters, Vol. 32, Issue 14, pp. 2007-2009* **32**, 2007–2009 (2007).

25. Tokunaga, M., Imamoto, N. & Sakata-Sogawa, K. Highly inclined thin illumination enables clear single-molecule imaging in cells. *Nature Methods 2008 5:2* **5**, 159–161 (2008).

26. Corbett, A. D. & Bub, G. Bringing the living brain into focus. *Nature Photonics 2015 9:2* **9**, 80–82 (2015).

27. Axelrod, D., Thompson, N. L. & Burghardt, T. P. Total internal reflection fluorescent microscopy. *J Microsc* **129**, 19–28 (1983).

28. Ambrose, E. J. A Surface Contact Microscope for the study of Cell Movements. *Nature 1956 178:4543* **178**, 1194–1194 (1956).

29. Maxwell, J. C. On the general laws of Optical Instruments. *The Scientific Papers of James Clerk Maxwell* 271–285 (2011) doi:10.1017/CBO9780511698095.020.

30. Microscope objectives: Back focal plane. https://amsikking.github.io/microscope_objectives/back_focal_plane.html.

31. Zhang, Y. & Gross, H. Systematic design of microscope objectives. Part I: System review and analysis. *Advanced Optical Technologies* **8**, 313–347 (2019).

32. Foreman, M. R. & Török, P. Computational methods in vectorial imaging. *J Mod Opt* **58**, 339–364 (2011).

33. Mariani, J. *et al.* FOXG1-Dependent Dysregulation of GABA/Glutamate Neuron Differentiation in Autism Spectrum Disorders. *Cell* **162**, 375–390 (2015).

34. Sousa, A. M. M., Meyer, K. A., Santpere, G., Gulden, F. O. & Sestan, N. Evolution of the Human Nervous System Function, Structure, and Development. *Cell* **170**, 226–247 (2017).

35. Mohamed, N.-V. *et al.* Generation of human midbrain organoids from induced pluripotent stem cells [version 2; peer review: 3 approved, 1 approved with reservations]. (2021) doi:10.12688/mniopenres.12816.1.

36. Richardson, D. S. *et al.* TISSUE CLEARING. *Nature reviews. Methods primers* **1**, (2021).

37. Edelstein, A., Amodaj, N., Hoover, K., Vale, R. & Stuurman, N. Computer Control of Microscopes using μManager. *Current protocols in molecular biology / edited by Frederick M. Ausubel ... [et al.]* **CHAPTER**, Unit14.20 (2010).

38. Edelstein, A. D. *et al.* Advanced methods of microscope control using μManager software. *J Biol Methods* **1**, e10 (2014).

39. Campbell, B. E., Mok, S. & Moraes, C. In Situ Measurement of Intra-tumoral Tissue Rigidity. in *The Tumor Microenvironment: Methods and Protocols* (ed. Ursini-Siegel, J.) 237–246 (Springer US, 2023). doi:10.1007/978-1-0716-2914-7_14.

40. amsikking/high_na_single_objective_lightsheet: Research article: High NA single-objective light-sheet (SOLS). Read here: https://andrewgyork.github.io/high_na_single_objective_lightsheet. https://github.com/amsikking/high_na_single_objective_lightsheet.

41. BIG • PSF Generator. http://bigwww.epfl.ch/algorithms/psfgenerator/#ref.

42. Kumar, M. *et al.* Integrated one- and two-photon scanned oblique plane illumination (SOPi) microscopy for rapid volumetric imaging. *Optics Express, Vol. 26, Issue 10, pp. 13027-13041* **26**, 13027–13041 (2018).

43. amsikking/SOLS_optimum_tilt: Calculations for choosing the tilt angle in a single-objective light-sheet (SOLS) microscope: https://amsikking.github.io/SOLS_optimum_tilt. https://github.com/amsikking/SOLS_optimum_tilt.

44. high_NA_lightsheet_by_AMSikking. https://andrewgyork.github.io/high_na_single_objective_lightsheet/.

45. Tissue Clearing Methods and Applications for Fluorescence Imaging- Oxford Instruments. https://andor.oxinst.com/learning/view/article/overview-of-tissue-clearing-methods-and-applications.

46. Susaki, E. A. *et al.* Whole-Brain Imaging with Single-Cell Resolution Using Chemical Cocktails and Computational Analysis. *Cell* **157**, 726–739 (2014).

47. Any_immersion_remote_refocus_microscopy_by_AMSikking. https://amsikking.github.io/any_immersion_remote_refocus_microscopy/.

48. Price, J. C., Roach, P. & El Haj, A. J. Liquid Crystalline Ordered Collagen Substrates for Applications in Tissue Engineering. *ACS Biomater Sci Eng* **2**, 625–633 (2016).

49. Hung, S.-T. *et al.* SOLEIL: single-objective lens inclined light sheet localization microscopy. *Biomedical Optics Express, Vol. 13, Issue 6, pp. 3275-3294* **13**, 3275–3294 (2022).

50. Hung, S. Te *et al.* Adaptive optics in single objective inclined light sheet microscopy enables three-dimensional localization microscopy in adult Drosophila brains. *Front Neurosci* **16**, 1622 (2022).

51. Park, S. *et al.* Restoring single-molecule localizations with wavefront sensing adaptive optics for deep-tissue super-resolution imaging. *bioRxiv* 2021.11.18.469175 (2021) doi:10.1101/2021.11.18.469175.

52. Wahl, D. J. *et al.* Wavefront sensorless adaptive optics versus sensor-based adaptive optics for in vivo fluorescence retinal imaging (Conference Presentation). *https://doi.org/10.1117/12.2253368* **10073**, 67–67 (2017).

53. Guo, Y. *et al.* Adaptive optics based on machine learning: a review. doi:10.29026/oea.2022.200082.

54. Saska, D. *et al.* μSPIM: A Software Platform for Selective Plane Illumination Microscopy. *bioRxiv* 2020.06.15.151993 (2020) doi:10.1101/2020.06.15.151993.

55. Chen, B. *et al.* Resolution doubling in light-sheet microscopy via oblique plane structured illumination. *Nature Methods 2022 19:11* **19**, 1419–1426 (2022).

56. Chen, B. *et al.* Increasing the field-of-view in oblique plane microscopy via optical tiling. *Biomedical Optics Express, Vol. 13, Issue 11, pp. 5616-5627* **13**, 5616–5627 (2022).

57. Pinkard, H. *et al.* Pycro-Manager: open-source software for customized and reproducible microscope control. *Nature Methods 2021 18:3* **18**, 226–228 (2021).

58. Sofroniew, N. *et al.* napari/napari: 0.4.13. (2022) doi:10.5281/ZENODO.5866555.

59. Cole, R. W., Jinadasa, T. & Brown, C. M. Measuring and interpreting point spread functions to determine confocal microscope resolution and ensure quality control. *Nature Protocols 2011 6:12* **6**, 1929–1941 (2011).

60. Abrams, B. *et al.* Tissue-Like 3D Standard and Protocols for Microscope Quality Management. *bioRxiv* 2022.08.14.503777 (2022) doi:10.1101/2022.08.14.503777.

61. Xing, J. F., Zheng, M. L. & Duan, X. M. Two-photon polymerization microfabrication of hydrogels: an advanced 3D printing technology for tissue engineering and drug delivery. *Chem Soc Rev* **44**, 5031–5039 (2015).

62. Harinarayana, V. & Shin, Y. C. Two-photon lithography for three-dimensional fabrication in micro/nanoscale regime: A comprehensive review. *Opt Laser Technol* **142**, 107180 (2021).

63. Ciuciu, A. I. & Cywí, P. J. Two-photon polymerization of hydrogels-versatile solutions to fabricate well-defined 3D structures. (2014) doi:10.1039/c4ra06892k.

A. Appendix

A.1. MATLAB code to generate recurring sinusoidal signal

```
d = daqlist("ni");
amplitude=0.3;%setting the amplitude of sinusoidal
offset=-0.85;%setting the offset of sinusoidal
deviceInfo = d{1, "DeviceInfo"};
dq = daq("ni");
dq.Rate = 2000;
addoutput(dq, "Dev2", "ao0", "Voltage");
outputSignal1 =offset+amplitude*sin((1:5000)*2*pi/5000);
start(dq,'repeatoutput');
write(dq,outputSignal1');
```

A.2. MATLAB code for synchronization and automated imaging

```
%% Parameter settings (From User input)
exposure=100;%in ms
scanstep=10;%in um
scanrange=400;%in um
FileName=User defined File name';

%% Parameter settings (Do not change)
centerV=-0.25;%in V, do not change unless microscope is re-calibrated
lagtime=2;%in ms
conversion=0.003232;%V/um
V_step=scanstep*conversion;%Voltage increment needed for each step
StartPoint=centerV-0.6;
EndPoint=StartPoint+scanrange*conversion;
OutputSignal=StartPoint-2*V_step:V_step:EndPoint+2*V_step;
fprintf('Total number of images: %d\n',length(OutputSignal));
mkdir(FileName);
```

```
%% Initiate NI DAQ communication

d = daqlist("ni");
deviceInfo = d{1, "DeviceInfo"};
dq = daq("ni");
dq.Rate = 3000;
addoutput(dq, "Dev2", "ao0", "Voltage");
write(dq,StartPoint);

%% Automated scanning
addpath(YOUR PATHWAY)
[rc] = AT_InitialiseLibrary();
AT_CheckError(rc);
[rc,hndl] = AT_Open(0);
AT_CheckError(rc);
disp('Camera initialized');
[rc] = AT_SetFloat(hndl,'ExposureTime',exposure/1000);
AT_CheckWarning(rc);
[rc] = AT_SetEnumString(hndl,'CycleMode','Fixed');
AT_CheckWarning(rc);
[rc] = AT_SetEnumString(hndl,'TriggerMode','Internal');
AT_CheckWarning(rc);
[rc] = AT_SetEnumString(hndl,'SimplePreAmpGainControl','16-bit (low noise & high well capacity)');
AT_CheckWarning(rc);
[rc] = AT_SetEnumString(hndl,'PixelEncoding','Mono16');
AT_CheckWarning(rc);


prompt = {'Enter Acquisition name','Enter number of images'};
dlg_title = 'Configure acquisition';
```

```
num_lines = 1;
def = {'acquisition','10'};
answer = inputdlg(prompt,dlg_title,num_lines,def);


filename = cell2mat(answer(1));
frameCount = str2double(cell2mat(answer(2)));

[rc] = AT_SetInt(hndl,'FrameCount',frameCount);
AT_CheckWarning(rc);

[rc,imagesize] = AT_GetInt(hndl,'ImageSizeBytes');
AT_CheckWarning(rc);
[rc,height] = AT_GetInt(hndl,'AOIHeight');
AT_CheckWarning(rc);
[rc,width] = AT_GetInt(hndl,'AOIWidth');
AT_CheckWarning(rc);
[rc,stride] = AT_GetInt(hndl,'AOIStride');
AT_CheckWarning(rc);
for X = 1:10
   [rc] = AT_QueueBuffer(hndl,imagesize);
   AT_CheckWarning(rc);
end
disp('Starting acquisition...');
[rc] = AT_Command(hndl,'AcquisitionStart');
AT_CheckWarning(rc);

i=0;
while(i<frameCount)
   % Move Galvo to target position
   write(dq, OutputSignal(i+1));
```

```
    pauses(lagtime/1000);

    % Capture image
    [rc,buf] = AT_WaitBuffer(hndl,1000);
    AT_CheckWarning(rc);
    [rc] = AT_QueueBuffer(hndl,imagesize);
    AT_CheckWarning(rc);
    [rc,buf2] = AT_ConvertMono16ToMatrix(buf,height,width,stride);
    AT_CheckWarning(rc);

    thisFilename = strcat(filename, num2str(i+1), '.tiff');
    disp(['Writing Image ', num2str(i+1), '/',num2str(frameCount),' to disk']);
    imwrite(buf2,"Local File Pathway"+FileName+thisFilename) %saves to desinated directory

    i = i+1;
end
disp('Acquisition complete');
[rc] = AT_Command(hndl,'AcquisitionStop');
AT_CheckWarning(rc);
[rc] = AT_Flush(hndl);
AT_CheckWarning(rc);
[rc] = AT_Close(hndl);
AT_CheckWarning(rc);
[rc] = AT_FinaliseLibrary();
AT_CheckWarning(rc);
disp('Camera shutdown');
write(dq,centerV-0.6);
```

A.3. Fiji script used for stack translation for 2D image reconstruction

```
xTranslate=2.05;
```

```
yTranslate=0;
/*Translate a stack of images so that the first image is moved n
pixels in the X direction, the second moved 2n pixels, the third 3n pixels
and so on..
the variable "n" is represented by xTranslate and yTranslate
*/
for(i=1;i<=nSlices;i++){
setSlice(i);
run("Translate...", "x="+i*xTranslate+" y="+i*yTranslate+" interpolation=Bilinear slice");
}
```

A.4. Notes for use of commercial software

Cobolt laser monitor:

- Manual shutter MUST BE CLOSED when turning on 561nm laser. 561nm is a diode pumped laser (DPL) which means it will perform a heat up when starting up. It will go up to its maximum power (85mW!!!) when starting up, CLOSE the manual shutter for everyone's safety
- Due to the nature of DPL laser, you will never get the exact power output as you targeted. It will always have 0.2-0.6mW deviation and it is small enough to be neglected
- The manual key must be turned off and back on when switching laser module. It is part of the designed safety lock
- DO not unplug the power for laser when finished using, simply turn off the laser and close the software. The laser module is designed to have the power cord plugged in when not using

Picard 4D USB stage:

- Before using the stage, make sure to move all X, Y and Z axis to the default reference point. You are risking go over the operating range by not doing so
- After finishing using the stage, make sure to home the stage in all X, Y and Z axis. The stage is guaranteed to go over its operating range after several imaging session if not doing so
- Be aware that the X, Y and Z axis on the sample stage is different from the conventional definition. Y-axis is the one moving up and down, so be careful not to make the sample collide with the objective

Bright-field camera:

- It is common for the software failing to find the hardware and having driver issue, simply restart the computer and it will be fixed
- Be aware that the camera may not be mounted in the nominal orientation, so upper side of the image may not correspond to the upper side of the world